

Article

Tetraruthenium Macrocycles with Laterally Extended Bis(alkenyl)quinoxaline Ligands and Their F₄TCNQ^{•−} Salts

Rajorshi Das ¹, Michael Linseis ¹, Laura Senft ², Ivana Ivanović-Burmazović ² and Rainer F. Winter ^{1,*} 

¹ Fachbereich Chemie, Universität Konstanz, Universitätsstraße 10, 78457 Konstanz, Germany; rajorshi.das@uni-konstanz.de (R.D.); michael.linseis@uni-konstanz.de (M.L.)

² Department Chemie, Ludwig-Maximilians-Universität München, Butenandtstraße 5-13, Haus D, 81377 München, Germany; laura.senft@cup.uni-muenchen.de (L.S.); ivana.ivanovic-burmazovic@cup.uni-muenchen.de (I.I.-B.)

* Correspondence: rainer.winter@uni-konstanz.de; Tel.: +49-7531-88-5355

Abstract: We report on the tetraruthenium macrocycles **Ru₄-5** and **-6** with a π -conjugated pyrene-appended 5,8-divinylquinoxaline ligand and either isophthalate or thiophenyl-2,5-dicarboxylate linkers and their charge-transfer salts formed by oxidation with two equivalents of F₄TCNQ. Both macrocyclic complexes were characterized by NMR spectroscopy, mass spectrometry, cyclic and square-wave voltammetry, and by IR, UV-vis-NIR, and EPR spectroscopy in their various oxidation states.

Keywords: metallamacrocycle; ruthenium; electrochemistry; spectroelectrochemistry; X-ray crystallography; charge-transfer salts



Citation: Das, R.; Linseis, M.; Senft, L.; Ivanović-Burmazović, I.; Winter, R.F. Tetraruthenium Macrocycles with Laterally Extended Bis(alkenyl)quinoxaline Ligands and Their F₄TCNQ^{•−} Salts. *Inorganics* **2022**, *10*, 82. <https://doi.org/10.3390/inorganics10060082>

Academic Editor: Marius Andruh

Received: 18 May 2022

Accepted: 11 June 2022

Published: 14 June 2022

Publisher's Note: MDPI stays neutral with regard to jurisdictional claims in published maps and institutional affiliations.



Copyright: © 2022 by the authors. Licensee MDPI, Basel, Switzerland. This article is an open access article distributed under the terms and conditions of the Creative Commons Attribution (CC BY) license (<https://creativecommons.org/licenses/by/4.0/>).

1. Introduction

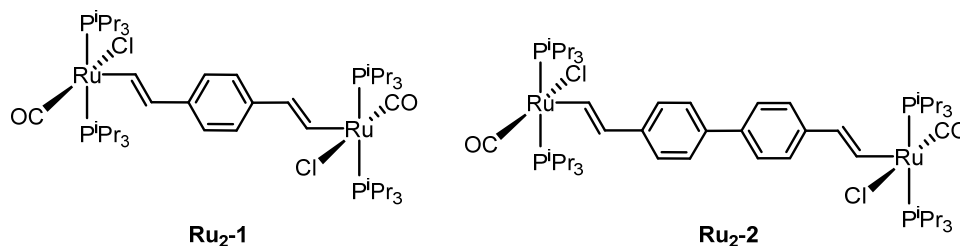
The incorporation of extended π -conjugated ligands into a supramolecular scaffold enhances its hydrophobicity and may lead to the selective uptake of guest molecules into their inner cavity through π -stacking interactions [1–9]. Apart from hydrophobic van der Waals interactions, electrostatic interactions arising from the different charge densities of the host and guest molecules also contribute significantly to stabilizing such donor-acceptor (D-A) compounds. The latter may exhibit new physical and chemical properties, including semiconductivity [10–13]. Therefore, supramolecular systems featuring π -extended electron-rich or -poor ligands have been a focal point of interest in recent years.

In previous work, we have demonstrated the ability of redox-active dinuclear ruthenium complexes with laterally π -extended bis(alkenyl)arylene ligands, such as they are present in compounds **Ru₂-3** and **-4** of Figure 1, to form charge-transfer (CT) salts with the strong organic electron acceptor 2,3,5,6-tetrafluoro-7,7,8,8-tetracyanoquinodimethane (F₄TCNQ, Figure 2). These salts showed enhanced stabilities, as compared to the ones prepared from complexes **Ru₂-1** and **Ru₂-2** with smaller arylene ligands [14]. We now wished to explore whether these dinuclear building blocks can be further elaborated into metallamacrocyclic structures. Macrocyclic tetraruthenium complexes of this general architecture are excellent examples of polyelectrochromic compounds, which can reversibly release up to eight electrons [15], depending on the carboxylate ligand, with intense absorption in the low-energy régime of the visible or the near infrared (NIR) in their various oxidized states, particularly those of a formally mixed-valent nature.

In the presence of dicarboxylates with a suitable disposition of the carboxylate functionalities, coordinatively unsaturated 14 valence electron diruthenium alkenyl complexes, which result from the abstraction of the chloride ligands from complexes of type **Ru₂-1** to **Ru₂-4**, offer the right compromise between the stability and lability of mono- and bidentate carboxylate bonding, in order to allow for the selective formation of tri-, tetra-, and hexaruthenium metallamacrocycles from initially formed mixtures of complexes with varying nuclearities [15–19]. The reversible formation and degradation of oligonuclear

complexes along the way to the thermodynamically most stable metallamacrocyclic or cage structure are highlighted by the selective transformation of intermittently formed tetra- or hexaruthenium metallamacrocycles into larger octa- or smaller tetraruthenium ones on prolonged warming, which is strongly accelerated in the presence of an excess of the respective carboxylate ligand [18–20]. Similar phenomena en route to supramolecular coordination compounds (SCCs) and interconversions between different types of defined metallamacrocyclic or cage architectures that originate from reversible ligand binding were also described for other complex/ligand combinations [21–30].

Ruthenium-alkenyl complexes without laterally extended π -conjugated systems



Ruthenium-alkenyl complexes with laterally extended π -conjugated systems

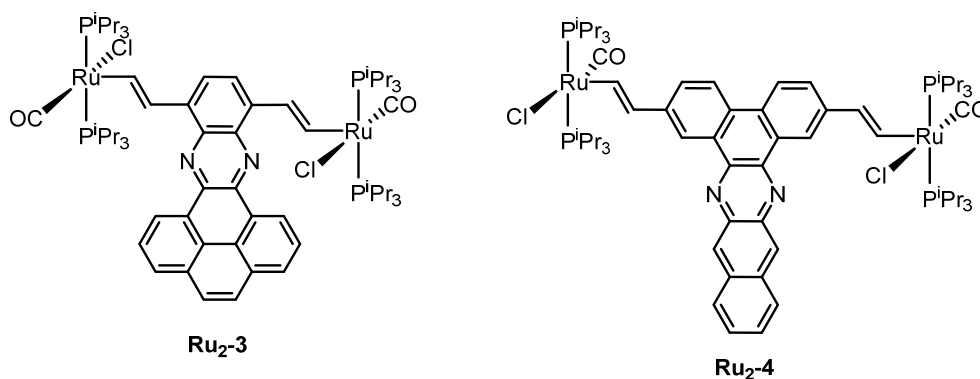


Figure 1. Dinuclear ruthenium-alkenyl complexes with and without laterally-extended π -conjugated arylene ligands.

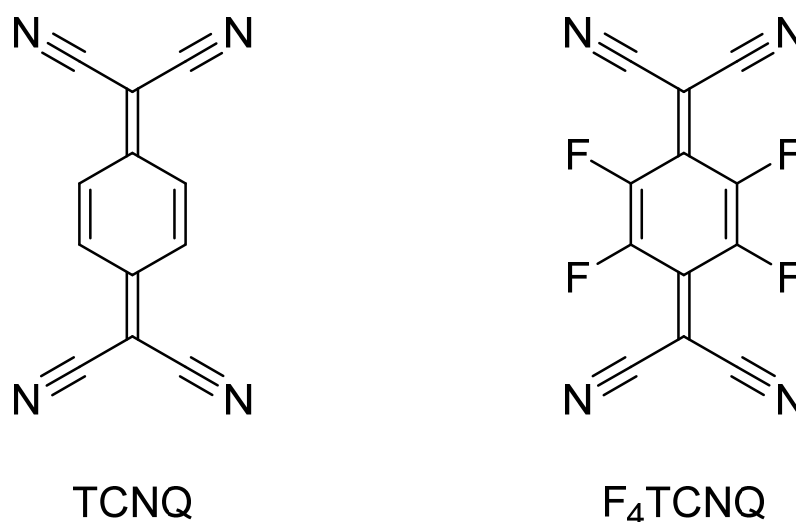


Figure 2. The commonly used organic electron-acceptors TCNQ (left) and F₄TCNQ (right).

Herein we report on two new tetraruthenium macrocycles, **Ru₄-5** and **Ru₄-6**, that result from the electron-rich diruthenium building block **Ru₂-3**. We mused that the presence of laterally-extended π -systems that protrude from both sides of such a macrocycle might allow for intermolecular $\pi \cdots \pi$ or $\text{CH} \cdots \pi$ interactions, which could aid in further associating individual molecules into higher-order structures, such as one-dimensional polymers [31,32]. In addition, the electron-rich ruthenium-alkenyl metalamacrocycles can donate electron(s) to strong organic electron acceptors, such as 7,7,8,8-tetracyanoquinodimethane (TCNQ) or its 2,3,5,6-tetrafluoro derivative F₄TCNQ (Figure 2), thereby providing charge-transfer complexes or radical salts that combine the open-shell forms of the macrocycles and one-electron reduced forms of the organic acceptor as their ionic constituents. Such tetraruthenium macrocycles may offer a platform that, upon associating with a planar acceptor, could form an extended columnar structure, where the donor (D) and acceptor (A) molecules alternate along the stacking axis. D-A-based charge-transfer salts with such a structure constitute an interesting class of hybrid materials that often exhibit (semi)conductive properties [33–37].

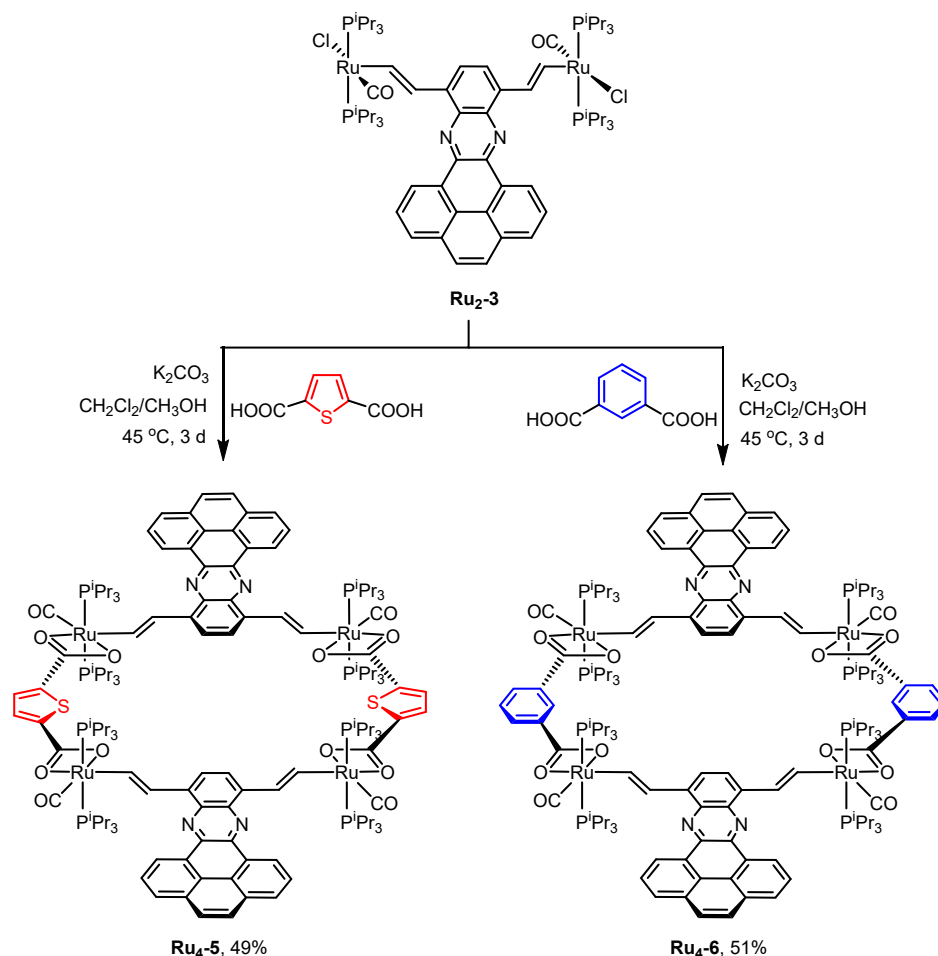
2. Results and Discussion

2.1. Synthesis and Spectroscopic Characterization

The macrocyclic tetraruthenium complexes were synthesized by reacting equimolar amounts of complex **Ru₂-3** and thiophene-2,5-dicarboxylic acid or benzene-1,3-dicarboxylic acid (isophthalic acid) as linkers in the presence of potassium carbonate and a solvent mixture of dichloromethane/methanol at 45 °C, according to a previously optimized procedure [15]. Completion of the reaction required three days and gave, after appropriate workup, the tetraruthenium macrocycles **Ru₄-5** and **Ru₄-6** in 49% or 51% yield as green solids (Scheme 1). The complexes are slightly air-sensitive and soluble in chlorinated solvents (dichloromethane and dichloroethane) and aromatic solvents (benzene and toluene). As solids, the complexes can be stored under inert conditions for months. However, they slowly degrade over two weeks in solution with lower stabilities in chlorinated solvents. The formation of the desired macrocycles was confirmed by multinuclear NMR spectroscopy (see Figures S1–S4 of the Supplementary Materials), ESI-MS, and X-ray crystallographic analysis of **Ru₄-5**. In the ¹H NMR spectra, the resonances of all aromatic and vinylic protons were observed in the expected chemical shift regions. For example, the vinyl protons of complex **Ru₄-5** appeared at 9.71 and 8.60 ppm, with the typical ³J_{H,H} coupling constant of 15.2 Hz. Similarly, the vinyl protons of **Ru₄-6** were observed at 9.74 and 8.84 ppm (³J_{H,H} = 15.5 Hz). The diruthenium building blocks and carboxylate bridging linkers showed only one set of resonances each, attesting to a symmetric structure (C₂ or D_{2h}) in solution. The ³¹P {¹H} NMR spectra of both complexes showed only a unique singlet resonance at $\delta = 38.62$ (**Ru₄-5**) or $\delta = 38.65$ ppm (**Ru₄-6**), which verified the *trans*-arrangement of the triisopropylphosphine ligands at the ruthenium ions.

The molecular compositions of tetranuclear macrocycles were confirmed by high-resolution electrospray-ionization mass spectrometry (HR-ESI MS). The mass peaks of the dications of complexes **Ru₄-5** and **Ru₄-6** constitute the base peaks of the experimental mass spectra. They were found at $m/z = 1423.9248$ (calculated for the [M]²⁺ ion of **Ru₄-5**, 1423.9371) and $m/z = 1417.9691$ (calculated for the [M]²⁺ ion of **Ru₄-6**, 1417.9809), respectively, with half-integer spacing between neighbouring isotopic peaks. Isotopic distributions of these peaks matched well with their simulated ones (see Figures S5–S8 in the Supplementary Materials). The mass peaks [M-H]⁺ of the parent monocations were also observed as much weaker signals at $m/z = 2847.8509$ (**Ru₄-5**) or $m/z = 2834.9369$ (**Ru₄-6**). Identified mass peaks of further macrocycle-derived fragments of **Ru₄-5** were located at $m/z = 1596.4055$ (**Ru₄-5**—[Ru(CO)Cl](P^{*i*}Pr₃)₃)₂(μ -CH=CH-BL-CH=CH) + 2H (BL = bridging pyrene-appended quinoxaline ligand) and $m/z = 1563.4437$, which is probably due to a fragment that derives from the former by loss of a sulfur atom from one of the dicarboxylic acids or a dicarboxylate diruthenium fragment with two attached BL ligands (see the Sup-

plementary Materials for further details). Other mass peaks of purely organic fragments without the ruthenium-specific isotope patterns could not be assigned unambiguously.



Scheme 1. Synthesis of tetraruthenium macrocycles **Ru₄-5** and **Ru₄-6**.

2.2. X-ray Crystallography

The formation and the proposed structure of macrocycle **Ru₄-5** were unambiguously confirmed by single-crystal X-ray diffraction analysis. Suitable crystals of the methanol tetrasolvate **Ru₄-5**·4 CH₃OH were obtained by layering a methanolic solution of the deprotonated dicarboxylate linker on top of a dichloromethane solution of **Ru₂-3**, with slow diffusion of the two layers over 2–3 days. The complex crystallized in the monoclinic space group *P*2₁/*c*. In the crystal, individual molecules adopt a *C*₁ symmetry that is lower as compared to the situation in fluid solution. The molecular structure is depicted in Figure 3.

As is shown in Figure 3A, the sulfur atoms of the thiophene heterocycles and oppositely-facing hydrogen atoms at the phenylene linkers define an inner void, with dimensions of 11.99 Å × 9.06 Å. They are, however, screened by the methyl protons of the P^{*i*}Pr₃ ligands, which provide smaller windows, with a width of ca. 6.3 Å to 6.6 Å. The four ruthenium atoms define a planar rhomboid, with Ru···Ru separations of 11.29 Å and 10.02 Å and internal angles of 81.22° and 98.78° (Figure 3C). The thiophene and quinoxaline rings of the dicarboxylate or divinylquinoxaline linkers are tilted by 6.3° or 12.6° out of this plane to alternate above or below the Ru₄ rhomboid, which endows the macrocycle with a somewhat wavy shape (Figure 3B). The torsion at the alkenyl linkages is only small, with Ru-C_{vinyl}-C_{vinyl}-C_{aryl} torsion angles of −172.3(9)° and −178.7(9)°. The ruthenium vinyl group associated with atom Ru1 is essentially coplanar with the phenylene linker, as shown by the torsional angles C_{vinyl}-C_{vinyl}-C_{aryl}-C_{aryl} of 177.3(11)° and −2.2(19)°, whereas that associated with Ru2 is rotated by a still modest margin of ca. 20° out of the phenylene

planes ($C_{\text{vinyl}}-C_{\text{vinyl}}-C_{\text{aryl}}-C_{\text{aryl}} = -164.5(11)^\circ$ and $-20.1(18)^\circ$, respectively). Such small torsion is beneficial for fostering electron delocalization over the π -conjugated diruthenium divinylquinoxaline entities. The *cisoid* arrangement of the two alkenyl groups, however, seems to introduce some strain within the macrocycle, which is accommodated by a rather strong torsion around the P-Ru \cdots Ru-P vectors of -18.8° and -21.3° , between *cis*-disposed P^iPr_3 ligands along the divinylarylene linkage (Figure 3B). No such torsion is present along the dicarboxylate linkage, as indicated by the P-Ru \cdots Ru-P angles of -1.2° and -1.3° , respectively. The annulated pyrene pendant at the 5,8-divinylquinoxaline linker shows a twist of 9.66° , as measured by the C-C-C-C torsion angle. This twisting is, however, largely confined to the site of annulation, as all other torsions of bonds between interconnected rings involving the 1,1'-biphenyl-type subunit within the pyrene skeleton are smaller than 2° ; only the one involving the outermost C-C linkage opposite the pyrazine heterocycle amounts to 2.50° . The Ru-C_{alkenyl} bond lengths of 1.965(10) and 1.967(10) Å agree well with the previously observed values (~ 1.977 Å) for other tetraruthenium-alkenyl macrocyclic complexes of the same general architecture [15,18,38].

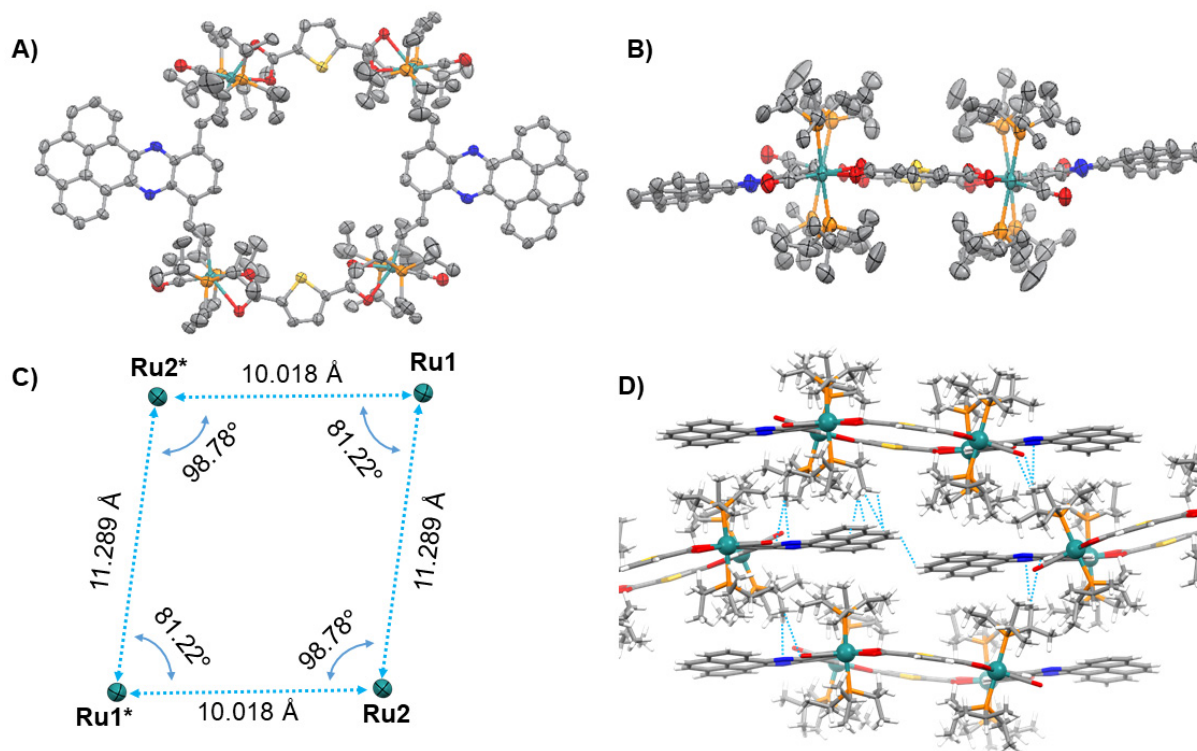


Figure 3. The structure of Ru₄-5 in Ru₄-5·4 CH₃OH. For Figures (A) (top view) and (B) (side view), solvent molecules and hydrogen atoms were removed for clarity reasons. (C) Intracycle Ru \cdots Ru distances and the inner angles of the tetraruthenium rhomboid. (D) Packing of individual molecules with intermolecular CH \cdots π interactions, indicated as light blue dotted lines. The ellipsoids are displayed at a 50% probability level. Colour codes: grey, carbon; red, oxygen; orange, phosphorous; white, hydrogen; green, chlorine; dark turquoise, ruthenium.

A peculiarity of this structure is the unequal binding of the two carboxylate functionalities at the thiophene-2,5-dicarboxylate linkers. One coordinates in the usual bidentate κ^2-O,O' binding mode with Ru–O bond lengths of 2.280(7) and 2.211(7) Å, with the longer bond to the O donor *trans* to the strongly σ -*trans*-influencing alkenyl ligand. The other carboxylate shows even more dissimilar Ru–O distances of 2.150(7) Å and 2.507(6) Å, suggesting only a weak Ru \cdots O interaction of Ru1 \cdots O3. Nevertheless, the bond lengths C–O of the carboxylate ligands show no significant differences and fall in a narrow range of 1.247(14) to 1.278(13) Å. The reason underlying this oddity is the formation of a hydrogen bond of carboxylate oxygen atom O3 and the OH proton of one of the cocrystallized

methanol solvent molecules with $d_{O \cdots O} = 2.782 \text{ \AA}$, which is 0.258 \AA shorter than the sum of their van der Waals radii. This methanol molecule is, in turn, associated with a second methanol solvent molecule to form an even shorter hydrogen bond with an $O \cdots O$ distance of 2.718 \AA (for a view see Figure S9 of the Supplementary Materials). Unequal carboxylate binding is also reflected in the different bond angles $O\text{--}Ru\text{--}C_{\text{alkenyl}}$ of $158.6(4)^\circ$ and $O\text{--}Ru\text{--}O$ of $59.0(2)^\circ$ for the regular bidentate or $147.8(4)^\circ$ and $55.5(2)^\circ$ for the other carboxylate functionality. Loose $Ru \cdots O_3$ binding also allows for a more ideal *trans* arrangement of the remaining carboxylate oxygen atom and carbonyl ligand, as shown by the larger $C\text{--}Ru\text{--}O$ angle of $174.9(4)^\circ$, as opposed to the corresponding one of $169.9(4)^\circ$ at the other Ru atom.

Although the pyrenyl pendants are directed toward the periphery of the macrocycle, they do not support intermolecular association by π -stacking. Rather, they engage in $CH \cdots \pi$ interactions with P^iPr_3 methyl hydrogen atoms, with a shortest contact of 2.844 \AA and with a methyl proton of the second methanol solvent molecule of 2.875 \AA and 2.790 \AA , respectively (see Figure 3D). As a result, individual molecules form a brick-wall type packing motif, which also allows for additional weak $CH \cdots \pi$ interactions to the quinoxaline heterocycle.

2.3. Electrochemistry

We next explored the electrochemical behaviour of the tetraruthenium macrocycles **Ru₄-5** and **Ru₄-6** by cyclic and square-wave voltammetry and compared it to that of the dichloro complex precursor **Ru₂-3**. Representative voltammograms in the THF/0.1 M $NBu_4^+ PF_6^-$ electrolyte are displayed in Figure 4. In this electrolyte, **Ru₂-3** displays two consecutive one-electron oxidations at $E_{1/2} = -68$ and 77 mV, which are dominated by the electron-rich divinylphenylene diruthenium part of this molecule, as well as a chemically partially reversible reduction at $E_{1/2} = -2085$ mV, which is biased toward the quinoxaline heterocycle [14]. Deviations of the closely spaced anodic waves from ideality seem to be due to some deposition of the oxidized forms of this complex onto the electrode surface of this electrolyte. In $CH_2Cl_2/NBu_4^+ PF_6^-$ (0.1 M), no such complication is encountered for the anodic waves. Half-wave potentials are shifted to -154 and 78 mV, thus showing an enhanced potential splitting of 232 mV, as opposed to 145 mV in THF. The improved behavior in anodic scans comes, however, at the expense of chemical irreversibility of the reduction (see Figure S10 of the Supplementary Materials).

This overall behaviour is fully retained in the macrocyclic counterparts **Ru₄-5** and **Ru₄-6**; only, each process now involves two electrons, as per the doubling of the number of the corresponding redox sites. All redox potentials are modestly shifted to more cathodic (more negative) potentials (Table 1), which is a consequence of the higher valence electron count of 18, as opposed to 16 at the ruthenium ions, and increased electron richness of the macrocycles (see Figure 4 and Table 1; further voltammograms and pertinent data are compiled in Figures S11–S16 and in Tables S2 and S3 of the Supplementary Materials). Close inspection of the individual anodic waves reveals a broadening, when compared to precursor **Ru₂-3**, indicating the presence of some slight redox splitting between the individual, merged one-electron waves. Individual half-wave potentials were estimated by digital simulation as ca. 80 and 60 mV for the first and second pair of oxidations, respectively (Table 1, see also Figures S13 and S16 of the Supplementary Materials) [39]. The small splitting for the first and second pair of one-electron oxidations of the divinylarylene diruthenium entities in such tetraruthenium metallamacrocycles has been traced to electrostatic, rather than electronic interactions [17,40,41]. Hence, they are mutually insulated from each other, as the dicarboxylate linkers do not support through-bond electronic coupling. This is also in accord with spectroscopic interrogations of their associated oxidized forms (see below).

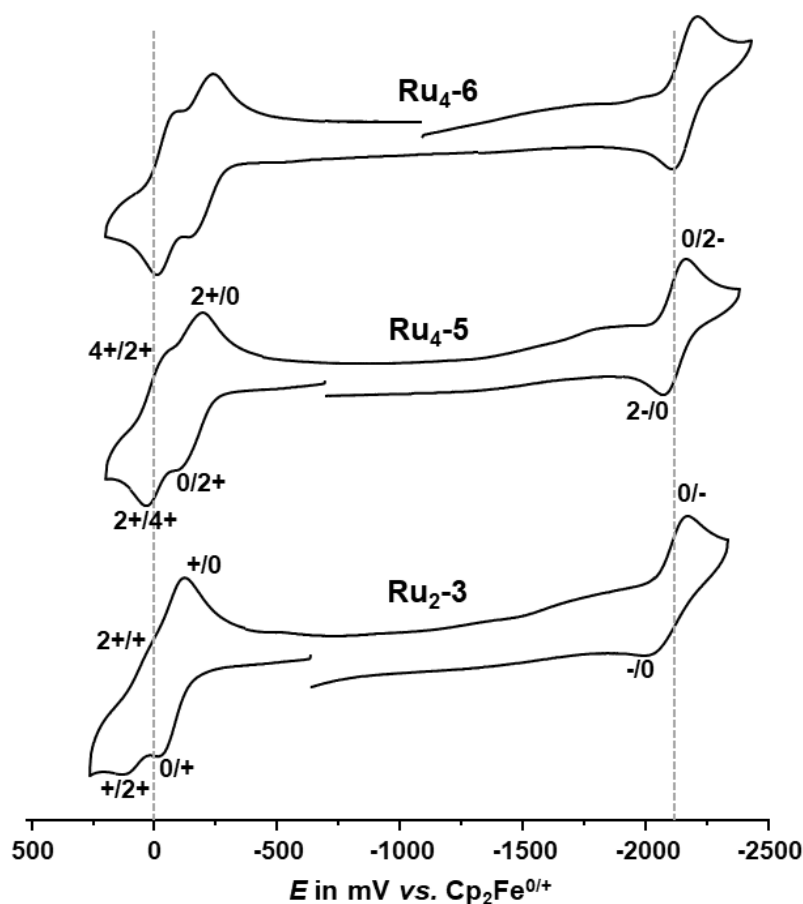


Figure 4. Cyclic voltammograms of **Ru₄-5**, **Ru₄-6**, and their diruthenium precursor **Ru₂-3** (THF, 0.1 M NBu₄⁺PF₆⁻, 295(±3) K, scan rate $v = 100$ mV/s). The dotted grey lines represent the (overall) half-wave potentials of the oxidations and reduction of complex **Ru₂-3**; they are intended as a guide to the eye.

Table 1. Cyclic voltammetric data of **Ru₂-3**, **Ru₄-5**, and **Ru₄-6**¹.

	$E_{1/2}^{0/+}$ (ΔE_p)	$E_{1/2}^{+/2+}$ (ΔE_p)	$E_{1/2}^{2+/3+}$ (ΔE_p)	$E_{1/2}^{3+/4+}$ (ΔE_p)	$\Delta E_{1/2}^{2+/4+}$	$E_{1/2}^{0/-}$ or $E_{1/2}^{0/2-}$ (ΔE_p)
Ru₂-3	−68 (111) [−154 (64)]	77 (104) [78 (67)]	—	—	145 [232]	−2085 (175) [−1510 (-)] ²
Ru₄-5	−134 (101) [−280 (-)] ³	−134 (101) [−200 (-)] ³	−6 (106) [−28 (-)] ³	−6 (106) [30 (-)] ³	128 [240]	−2120 (96) [−2074 (128)] ²
Ru₄-6	−174 (102) [−320 (-)] ³	−174 (102) [−240(-)] ³	−36 (89) [−66(-)] ³	−36 (89) [−10(-)] ³	138 [240]	−2159 (102) [−2118(157)] ²

¹ All data in millivolts versus Cp₂Fe^{0/+} in THF/NBu₄PF₆ (0.1 M) [CH₂Cl₂/NBu₄PF₆ (0.1 M)] at r. t. and at $v = 100$ mV/s. ² Peak potential of a chemically irreversible process. ³ Estimated by digital simulation of experimental voltammograms [39].

2.4. IR and UV–vis–NIR Spectroelectrochemistry

Changes of electron densities at the ruthenium nodes of the macrocycles, as a consequence of a redox process, were readily monitored by the stepwise shifts of the CO stretching vibrations of the bound carbonyl ligands. For a genuinely ruthenium-centred oxidation, the latter were expected to blue-shift by ca. 120 cm⁻¹ [42]. Attenuated shifts indicate enhanced ligand contribution (here, of the bridging bis(alkenyl)arylene linker) to the corresponding redox orbital [43,44]. Besides gauging the metal/ligand contribution to the redox process, the charge-sensitive Ru(CO) tag is also a highly convenient probe for electron delocalization within a mixed-valent [(CO){M}-BL-{M}(CO)]ⁿ⁺ entity (BL = bridging ligand), where the metal-coligand constituents {M} adopt (formally) dif-

ferent oxidation states. We have made extensive use of this tool in previous forays into π -conjugated divinylarylene-diruthenium complexes [45–48]. In order to scrutinize the present metallamacrocycles accordingly, we generated their corresponding oxidized forms by electrolysis inside an optically transparent thin-layer electrochemical (OTTLE) cell, as developed by Hartl et al. [49], or chemical reaction with a suitable oxidizing agent at the required stoichiometry [50]. Results of these studies are displayed in Figures 5 and 6, as well as in Figures S17–S25 of the Supplementary Materials; relevant data are collected in Table 2.

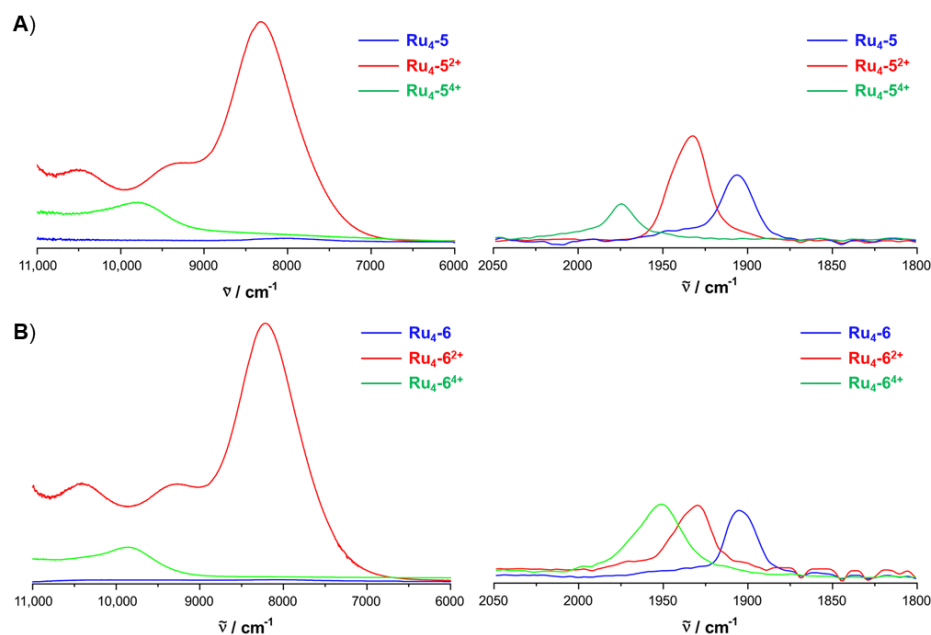


Figure 5. Spectroscopic changes in the mid-IR [Ru(CO)] and NIR spectra of (A) Ru₄-5 (blue) upon oxidation to [Ru₄-5]²⁺ (red) and [Ru₄-5]⁴⁺ (green) and (B) of Ru₄-6 (blue) upon oxidation to [Ru₄-6]²⁺ (red) and [Ru₄-6]⁴⁺ (green) in CH₂Cl₂ at 298 K (*c* = 80 mM). The dications [Ru₄-5]²⁺ or [Ru₄-6]²⁺ and tetracations [Ru₄-5]⁴⁺ or [Ru₄-6]⁴⁺ were obtained by treatment of the neutral macrocycle with 2 equivalents of ferrocenium hexafluorophosphate (Fc⁺ PF₆[−]) or 4 equivalents of acetylferrocenium hexafluoroantimonate (AcFc⁺ SbF₆[−]), respectively.

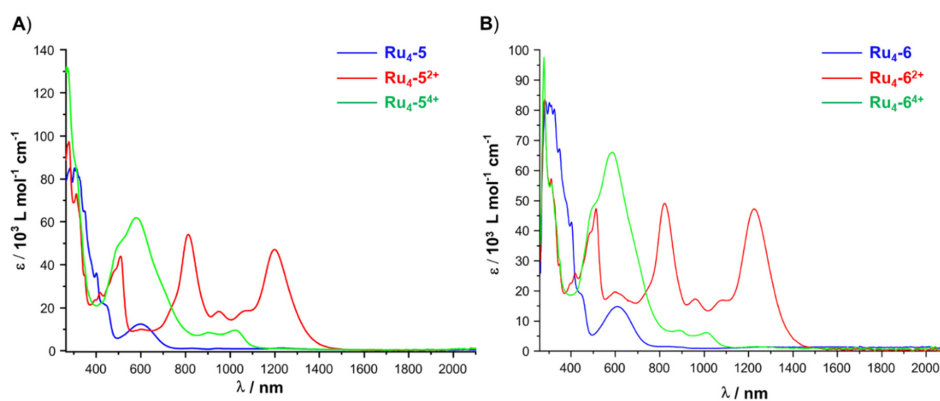


Figure 6. Spectroscopic changes in the UV-vis-NIR spectra of (A) Ru₄-5 (blue) upon the oxidation to [Ru₄-5]²⁺ (red) and [Ru₄-5]⁴⁺ (green) and (B) of Ru₄-6 (blue) upon oxidation to [Ru₄-6]²⁺ (red) and [Ru₄-6]⁴⁺ (green) in CH₂Cl₂ at 298 K (*c* = 80 mM). The dications [Ru₄-5]²⁺ and [Ru₄-6]²⁺ and tetracations [Ru₄-5]⁴⁺ and [Ru₄-6]⁴⁺ were obtained by treatment of the neutral macrocycle with 2 equivalents of ferrocenium hexafluorophosphate (Fc⁺ PF₆[−]) or 4 equivalents of acetylferrocenium hexafluoroantimonate (AcFc⁺ SbF₆[−]), respectively.

Table 2. IR–NIR and UV–vis–NIR spectroscopic data of the compounds **Ru₂-3**, **Ru₄-5**, and **Ru₄-6** in their neutral, dicationic, and tetracationic states [a].

	ν_{CO} (cm ⁻¹)	λ (nm) (ϵ_{max} [M ⁻¹ cm ⁻¹])
Ru₂-3	1912	351 (48,000), 400 (26,300), 597 (11,200)
[Ru₂-3]⁺	1934, 1945 (sh)	350 (33,700), 452 (17,000), 512 (17,700), 602 (20,500), 814 (8800), 947 (5500), 1220 (7900)
[Ru₂-3]²⁺	1955	349 (35,000), 451 (14,400), 564 (1,3000), 1009 (9800)
Ru₄-5	1906	312 (84,500), 347 (65,000), 403 (36,000), 444 (22,200), 599 (12,400)
[Ru₄-5]²⁺	1932, 1946	312 (73,000), 349 (35,200), 417 (27,100), 482 (37,500), 509 (44,000), 811 (54,000), 950 (18,300), 1065 (18,700), 1200 (47,000)
[Ru₄-5]⁴⁺	1973	306 (87,000), 347 (40,000), 505 (50,000), 576 (62,000), 900 (8450), 1020 (9700)
Ru₄-6	1905	285 (83,000), 302 (82,500), 311 (82,000), 324 (80,000), 348 (67,200), 402 (42,800), 445 (19,000), 606 (14,800)
[Ru₄-6]²⁺	1930, 1940	311 (55,840), 418 (26,000), 488 (39,500), 512 (47,100), 598 (19,700), 818 (50,000), 960 (17,300), 1084 (17,000), 1222 (47,200)
[Ru₄-6]⁴⁺	1952	278 (97,500), 315 (55,000), 494 (47,400), 585 (66,000), 890 (6900), 1010 (6200)

[a] Measurements were carried out in either CH₂Cl₂ or CH₂Cl₂/0.1 M NBu₄⁺ PF₆⁻ at room temperature.

Further oxidation to the associated tetracations leads to an additional blue shift of the Ru(CO) band to 1973 or 1952 cm⁻¹, respectively, as well as the bleach of the IVCT band. As is always observed in these complexes, the average CO band shift per one-electron oxidation at each half of the diruthenium divinylphenylene entity of 67 or 47 cm⁻¹ falls significantly short of the value of 120 cm⁻¹, which is expected for a ruthenium-centred oxidation [42]. This is a token of the large contribution of the bis(alkenyl)arylene ligand to the HOMO of these complexes.

Besides the appearance and bleaching of the NIR IVCT band, the stepwise oxidations lead to further changes in the electronic spectra of the macrocycles, as is shown in Figure 6. Neutral **Ru₄-5** and **Ru₄-6** show three distinct bands in their Vis spectra, one close to 400 nm, one at ca. 445 nm, and one close to 600 nm. All these bands have no equivalents in the simple divinylphenylene-bridged diruthenium complexes {(L)(PⁱPr₃)₂(CO)Ru}₂(-CH=CH-C₆H₄-CH=CH) with L = Cl⁻, RCOO⁻, or acac⁻ [14,44]; hence, they must originate from the lateral extension of the bridging aryene ligand. Quantum chemical calculations on a simplified PMe₃ model of complex **Ru₂-3** (further on denoted as ^{Me}**Ru₂-3**) duly indicate that they are associated with intraligand charge transfer from either the electron-rich diruthenium divinylphenylene entities to the pyrazine and annulated pyrene rings, with varying contributions of these two units, or from pyrene to the quinoxaline heterocycle. Figure 7 provides the computed UV–vis spectrum and electron density difference maps for the individual transitions that visualize the accompanying shifts in electron densities. Contour diagrams of the molecular orbitals that are involved in these transitions can be found in Figure S26 of the Supplementary Materials. A red shift of particularly the band at ca. 400 nm in the present macrocycles from its position of 351 nm in **Ru₂-3** is likely a consequence of the higher electron richness (hence, the higher energy of the relevant occupied donor levels) on coordinative saturation, and this was similarly observed for the corresponding acac⁻ derivative of **Ru₂-3** [14].

The first overall two-electron oxidation changes the neutral 5,8-divinylquinoxaline-diruthenium entities to their corresponding one-electron oxidized radical cations. It is, thus, accompanied by the growth of the characteristic electronic absorptions of the open-shell metal-organic chromophore at 509, 811, and 1200 nm (**[Ru₄-5]²⁺**) or 512, 818, and 1222 nm (**[Ru₄-6]²⁺**), with additional weaker bands. These oxidation-induced alterations provide a close match to the observations for the one-electron oxidized forms of their dinuclear precursor **[Ru₂-3]^{•+}** and its acac⁻ derivative [14]. The NIR band at the lowest energy is identical to the one already observed in the IR–NIR spectra. Particularly in the case of the present complexes, this NIR transition was not strictly confined to the divinylphenylene diruthenium entity, but was accompanied by a flow of electron density from the annulated pyrene to the latter, as is indicated by our quantum chemical calculations on the singly oxidized model complex [^{Me}**Ru₂-3]^{•+}** (see Figure 8). It is, hence, better described as an

intraligand charge-transfer (ILCT) band, rather than as a classical intervalence charge-transfer (IVCT) excitation. The same assignment also holds for the band near 510 nm. We note that the donor and acceptor orbitals for both transitions are symmetrically distributed over the two fragment halves, with equal contributions from the two vinylruthenium moieties. This is in line with the idea of the complete charge delocalization within each of the mixed-valent divinylquinoxaline diruthenium entities of the macrocycles, just as it was inferred from the pattern of the Ru(CO) bands.

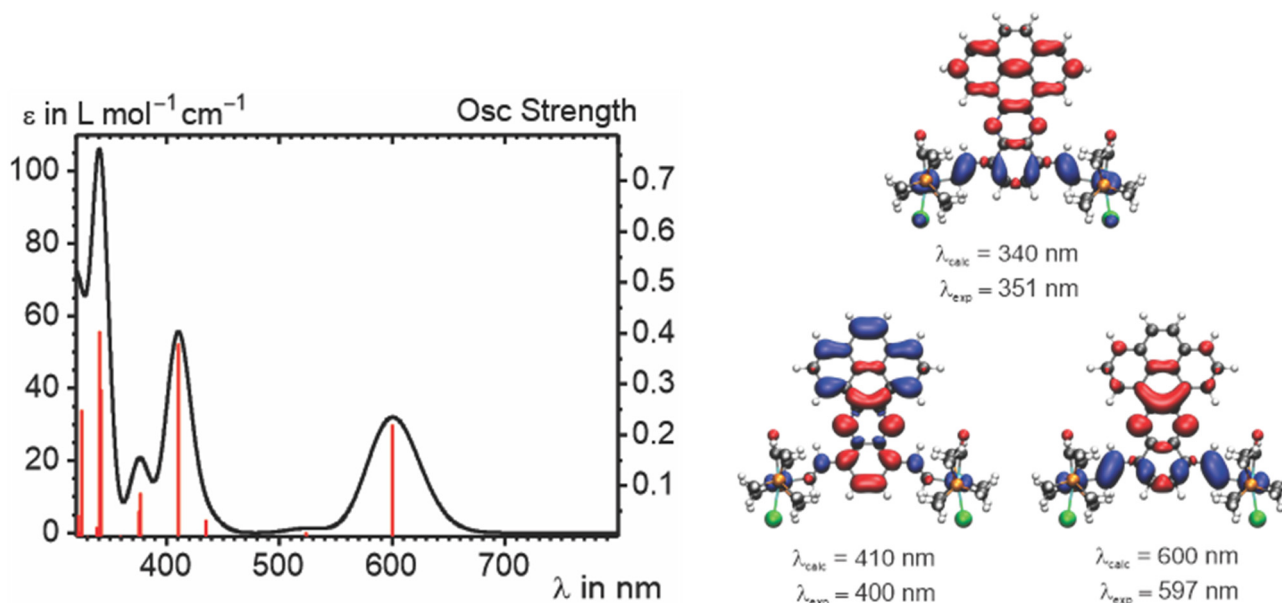


Figure 7. (Left): Calculated UV-vis-NIR spectrum of model complex $\text{MeRu}_2\text{-3}$ obtained from TD-DFT calculations. (Right): Electron density difference maps (EDDMs) for the three main electronic transitions in the visible/near UV. The red colour marks an increase and blue colour marks a decrease of electron density during the corresponding electronic transition.

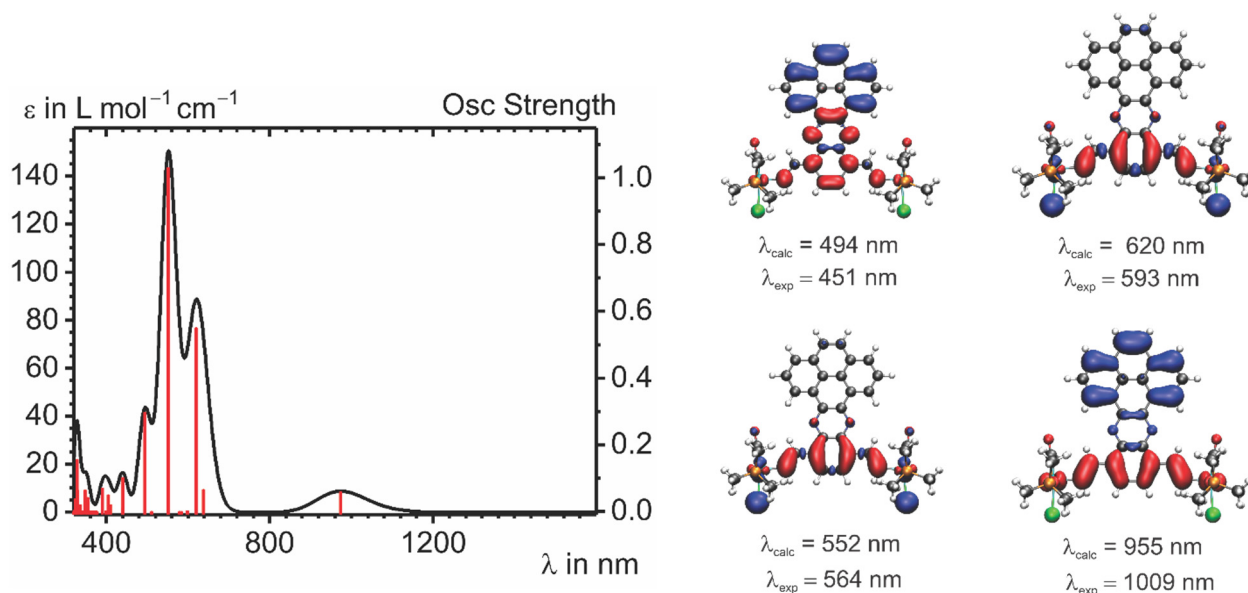
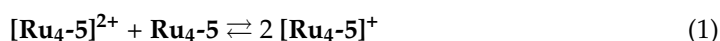


Figure 8. (Left): Calculated UV-vis-NIR spectrum of the model complex $[\text{MeRu}_2\text{-3}]^{\bullet+}$ obtained from the TD-DFT calculations. (Right): Electron density difference maps (EDDMs) for the four main electronic transitions in the visible-near UV. The red colour marks an increase and blue colour marks a decrease of electron density during the corresponding electronic transition.

Revealingly, at no stage during the gradual conversion of the neutral to dicationic forms of the macrocyclic complexes have we observed any additional NIR band that would relate to IVCT between the oxidized and reduced divinylquinoxaline diruthenium sides in a mono-oxidized intermediate, where both are present within the same molecule. Such a band would be expected to increase during the initial, and then decrease during the later stages of the overall two-electron oxidation (for close-up views of this spectral region, see Figure S21 of the Supplementary Materials). As dictated by the comproportionation equilibrium in Equation (1), the radical cations will be present in quantities that would allow for their detection, had they any specific absorption band [16]. Here, one should note that, even in the absence of any detectable half-wave potential splitting between the 0/+ and +/2+ redox couples, that is when the redox potentials $E_{1/2}^{0/+}$ and $E_{1/2}^{+/2+}$ were identical, a total of 25% of the neutral and the oxidized macrocycles each, and 50% of the one-electron oxidized radical cations are present within the diffusion layer after one equivalent of charge had been released (Equation (2); K_{comp} denotes the equilibrium constant for the comproportionation reaction). The absence of an additional IVCT band, thus, indicates that the two divinylarylene diruthenium subunits are mutually insulated from each other and that the dicarboxylate linkers just serve as physical links, but do not allow for any through-bond delocalization. This is not surprising, considering the identical behaviour of other tetraruthenium macrocycles of the same general constitution and with the same or similar dicarboxylate linkers [15,17,38,40].



$$K_{\text{comp}} = \exp \left\{ (F/RT) \cdot (E_{1/2}^{+/2+} - E_{1/2}^{0/+}) \right\} \quad (2)$$

Upon further oxidation of the macrocycles to their corresponding tetracations, the ILCT band retains its character, but shows a decreased intensity and is shifted to higher energy (lower wavelength), i.e., ca. $10,000 \text{ cm}^{-1}$ (1000 nm). Another characteristic asset of the four-fold oxidized macrocycles $[\text{Ru}_4\text{-5}]^{4+}$ and $[\text{Ru}_4\text{-6}]^{4+}$ is the intense structured absorption that peaks at ca. 580 nm. The discernible shoulder superimposed at the low-energy side and more distinct additional feature near 500 nm suggest that the absorption envelope entails more than one electronic transition. Our calculations on $[\text{MeRu}_2\text{-3}]^{2+}$ reproduce this pattern very well and provide three separate transitions of mainly a ligand-to-ligand' or intraligand charge-transfer character from either the peripheral donor ligands at the ruthenium ions or the pyrene portion of the bridging ligand to the oxidized divinylphenylene linker. The computed electronic spectrum and electron density difference maps for the individual excitations are collected in Figure S27 of the Supplementary Materials.

2.5. EPR Spectroscopic Studies

For the purpose of EPR spectroscopic investigations, the dications $[\text{Ru}_4\text{-5}]^{2+}$ and $[\text{Ru}_4\text{-6}]^{2+}$, as well as the reduced forms $[\text{Ru}_4\text{-5}]^{2-}$ and $[\text{Ru}_4\text{-6}]^{2-}$, were generated by oxidizing the neutral compounds with two equivalents of ferrocenium hexafluorophosphate in dichloromethane at room temperature or a chemical reduction with two equivalents of decamethylcobaltocene in THF. As expected, the dications with two singly oxidized divinylquinoxaline diruthenium entities provide an intense, yet unresolved EPR signal at g -values of 2.010 or 2.020, respectively, without any detectable hyperfine splittings to other nuclei. Experimental spectra are shown in Figures S28–S30 of the Supplementary Materials. The tetracations of macrocycles **Ru₄-5** and **Ru₄-6** were obtained by using four equivalents of the stronger oxidant acetylferrocenium hexafluoroantimonate. Similar to the dications, the tetracations $[\text{Ru}_4\text{-5}]^{4+}$ and $[\text{Ru}_4\text{-6}]^{4+}$ also showed an isotropic signal at $g = 2.019$, yet with considerably smaller intensity and distinctly larger half-width when compared to the dications. Such behaviour has been traced to a near degeneracy between an open-shell ground and a closed-shell excited state of their dioxidized divinylarylene diruthenium constituents [17,48]. The spin density in the associated radical anion is also ligand-based, which is in accord with the composition of the LUMO of the model complex

$\text{MeRu}_2\text{-3}$ (see Figure S26 of the Supplementary Materials). It is characterized by an isotropic, likewise unresolved resonance signal with a lower g value of 1.9889 or 1.9899, respectively (see Figure S30 of the Supplementary Materials). Spin density plots for all three different charge states of the diruthenium precursor complex $[\text{MeRu}_2\text{-3}]^{n+}$ are shown in Figure S31 of the Supplementary Materials and support the notion of (mainly) bridge-centred redox processes with no (reduced form) or small (cation, dication in the EPR-active triplet state) ruthenium contribution.

3. Charge-Transfer Salts of the Macrocycles

Utilizing the low oxidation potentials of the electron-rich tetraruthenium macrocycles, we have synthesized their radical salts by treatment with the strong organic electron acceptor F_4TCNQ ($\text{F}_4\text{TCNQ} = 2,3,5,6\text{-tetrafluoro-7,7,8,8-tetracyanoquinodimethane}$). F_4TCNQ is a widely used electron acceptor, due to the particularly low energy level of its LUMO (lowest unoccupied molecular orbital) and high chemical stability of its reduced mono- and even dianionic forms [51–55]. The addition of two equivalents of F_4TCNQ to dichloromethane solutions of complexes $\text{Ru}_4\text{-5}$ and $\text{Ru}_4\text{-6}$ yielded the salts **CT-1** and **-2**, as indicated by an immediate colour change to yellow-green (see Figures S32–S34 of the Supplementary Materials). The formation of the salts can be easily monitored by IR, UV–vis–NIR, and EPR spectroscopy. In particular, the UV–vis–NIR spectra of these salts showed the characteristic bands of the dicationic forms of the macrocyclic complexes $[\text{Ru}_4\text{-5}]^{2+}$ and $[\text{Ru}_4\text{-6}]^{2+}$, as well as those of the monoreduced $[\text{F}_4\text{TCNQ}]^{\bullet-}$ anion at 752 and 852 nm, which are better resolved from a partially overlapping band of the dioxidized macrocycle in **CT-1** (Figure 9A and Figure S35 of the Supplementary Materials). EPR spectra likewise displayed the separate broader resonance signal of the macrocycle dication and sharper one of the $[\text{F}_4\text{TCNQ}]^{\bullet-}$ anion in both the fluid solution and solid state. The experimental and simulated EPR spectra of salts **CT-1** and **CT-2** (dichloromethane, r. t.) are depicted in Figure 9B and Figure S36 of the Supplementary Materials. The complex cations are associated with g -values of 2.023 (for the $[\text{Ru}_4\text{-5}]^{2+}$ constituent of **CT-1**) or 2.024 (for the $[\text{Ru}_4\text{-6}]^{2+}$ dication of **CT-2**), whereas that of the $[\text{F}_4\text{TCNQ}]^{\bullet-}$ anion was found at $g = 1.9876$. Characteristic changes are also seen in the IR spectra. Hence, the $\text{Ru}(\text{CO})$ band of the oxidized complexes at ca. 1930 cm^{-1} was found alongside the $\text{C}\equiv\text{N}$ stretches of the $[\text{F}_4\text{TCNQ}]^{\bullet-}$ anion at 2194 and 2174 cm^{-1} , which were considerably red-shifted from those of pristine F_4TCNQ at 2226 and 2213 cm^{-1} . The observed values well match those in the literature [56–60].

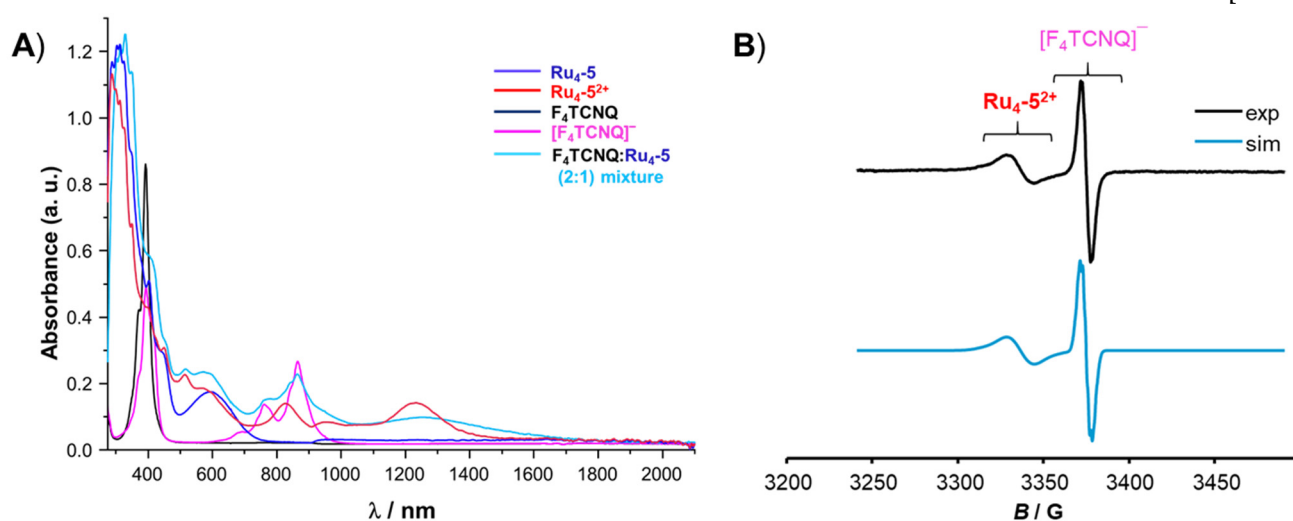


Figure 9. (A) UV–vis–NIR and (B) EPR spectra of salt **CT-1** synthesized by the reaction of 2 equivalents of F_4TCNQ with $\text{Ru}_4\text{-5}$ in CH_2Cl_2 at 298K. The experimental spectrum is shown at the top and the simulated one at the bottom.

4. Materials and Methods

Experimental Methods and Materials. All manipulations were performed under an atmosphere of purified nitrogen with dry, distilled, and nitrogen-saturated solvents. All reagents were purchased from commercial sources and were used without further purification. ^1H NMR (400 MHz) and ^{31}P NMR (162 MHz) spectra were recorded on a Bruker Avance III 400 spectrometer. The dinuclear ruthenium complex **Ru₂-3** was synthesized following the published procedure [14]. Thiophene-2,5-dicarboxylic acid and isophthalic acid were purchased from Fluorochem Ltd. and Sigma Aldrich.

Mass spectra were recorded on an UHR-ToF Bruker Daltonik (Bremen, Germany) maXis ESI-quadrupole time-of-flight (qToF) mass spectrometer, with a resolution better than 60,000 full width at half-maximum (fwhm). The N_2 drying gas was heated to 180 °C, while the spray gas temperature was 20 °C. Signal detection was performed in the positive-ion mode at a 4.5 kV voltage. Calibration with ESI-ToF low concentration tuning mix of Agilent was performed prior to every measurement. All measurements were performed on CH_2Cl_2 solutions of the respective complex.

Electrochemical and Spectroelectrochemical Measurements. All electrochemical experiments were performed in a custom-made, cylindrical, vacuum-tight, one-compartment cell. Spiral-shaped Pt and Ag wires, as the counter and reference electrodes, were sealed into glass capillaries that were introduced via Quickfit screws at opposite sides of the cell. A platinum electrode was introduced as the working electrode through the top port via a Teflon screw cap with a suitable fitting. It was polished first with 1 μm and then 0.25 μm diamond pastes from Buehler-Wirtz before the measurements. The cell can be attached to a conventional Schlenk line via a side arm equipped with a Teflon screw valve. The cell allowed experiments to be performed under an atmosphere of argon with approximately 6 mL of analyte solution. $\text{NBu}_4^+ \text{PF}_6^-$ was used as a supporting electrolyte.

Referencing was performed by the addition of decamethylferrocene (Cp^*Fe) as an internal standard to the analyte solution, after all data of interest had been acquired. Representative sets of scans were repeated with the added standard. Final referencing was performed against the ferrocene/ferrocenium ($\text{Cp}_2\text{Fe}^{0/+}$) couple, with $E_{1/2}(\text{Cp}^*\text{Fe}^{0/+}) = -550$ mV vs. $E_{1/2}(\text{Cp}_2\text{Fe}^{0/+})$ in dichloromethane or -495 mV vs. $E_{1/2}(\text{Cp}_2\text{Fe}^{0/+})$ in tetrahydrofuran with $\text{NBu}_4^+ \text{PF}_6^-$ as the supporting electrolyte. Electrochemical data were acquired with a computer-controlled BASi potentiostat.

The optically transparent thin-layer electrolysis (OTTLE) cell was also custom-made and comprised Pt-mesh working and counter electrodes and thin silver wire as a pseudoreference electrode sandwiched between the CaF_2 windows of a conventional liquid IR cell. Its design followed that of Hartl et al. [49]. The working electrode was positioned in the centre of the spectrometer beam. Digital simulation of the cyclic voltammograms was conducted with DigiSim3, Version 3.03 [39].

Spectroscopic Measurements. FT-NIR spectra were recorded on a Bruker Tensor III instrument. UV-vis-NIR spectra were obtained on a TIDAS fiberoptic diode array spectrometer (combined MCS UV/vis and PGS NIR instrumentation) from j&m in HELLMA quartz cuvettes with 0.1 cm optical path lengths. Electron paramagnetic resonance (EPR) studies were performed on a table-top X-band spectrometer MiniScope MS 400 from Magnetec equipped with the matching temperature controller model H03a and a frequency counter Fc 400. Simulation of the experimental EPR spectra was performed with the MATLAB EasySpin program [61]. All measurements were performed at room temperature, and the macrocycles were chemically oxidized using ferrocenium hexafluorophosphate ($\text{Cp}_2\text{Fe}^+ \text{PF}_6^-$) or acetylferrocenium hexafluoroantimonate ($\text{AcCp}_2\text{Fe}^+ \text{SbF}_6^-$) as oxidizing agents. Reduction of the complexes was conducted inside a nitrogen-filled glovebox MBraun by adding THF to a mixture of the corresponding macrocyclic complexes and 2 equivalents of decamethylcobaltocene.

X-Ray Crystallography.

X-Ray diffraction analysis was performed on a STOE IPDS-II diffractometer (STOE & CIE GmbH, Darmstadt, Germany) equipped with a graphite monochromated $\text{MoK}\alpha$

radiation source ($\lambda = 0.71073 \text{ \AA}$) and an image plate detection system at $T = 100.15 \text{ K}$. Using *Olex2* [62], the structures were solved with the *SHELXT* [63] structure solution program using intrinsic phasing and refined with the *SHELXL* [63] refinement package using least squares minimization. Hydrogen atoms were introduced at their calculated positions. Structure plots were generated with the *ORTEP* program [64].

CCDC number 2,172,028 (for **Ru₄-5**) contains the supplementary crystallographic data, which is available free of charge by the joint Cambridge Crystallographic Data Centre and Fachinformationszentrum Karlsruhe. The best out of several selected crystals of complex **Ru₄-5** was a small, very thin platelet, with a particularly small size in one dimension. Even an extended measurement time of 45 min per frame did not give reflexes with reasonable intensity above $2\theta = 40^\circ$, so that the measurement was only performed to $\theta = 45^\circ$. This generated a level A alert, as the value of $\sin(\theta_{\max})/\lambda$ was less than 0.550.

Powder X-ray diffraction (PXRD) measurements were carried out with a BrukerD8 Discover device with a $1 \mu\text{S}$ microfocus X-ray source ($\text{CuK}\alpha$) equipped with an energy dispersive LynxEye detector. The sample holder was oscillated during the measurement, and the samples were measured from $5^\circ \leq 2\theta \leq 70^\circ$.

Computational Details. The ground state electronic structures were calculated by density functional theory (DFT) methods using the Gaussian 09 program packages [23]. Open shell systems were calculated by the unrestricted Kohn–Sham approach (UKS). Geometry optimization followed by vibrational analysis was performed in solvent media. Solvent effects were described by the polarizable continuum model (PCM) with standard parameters for 1,2-dichloroethane [65,66]. The quasirelativistic Wood-Boring small-core pseudopotentials (MWB) [67,68], and the corresponding optimized set of basis functions for Ru [69] and 6-31G(d) polarized double- ξ basis sets [70] for the remaining atoms were employed, together with the Perdew, Burke, and Ernzerhof exchange and correlation functional (PBE0) [71,72]. The GaussSum program package was used to analyze the results [73], while the visualization of the results was performed with the Avogadro program package [74]. Graphical representations of molecular orbitals were generated with the help of GNU parallel [75] and plotted using the vmd program package [76], in combination with POV-Ray [77].

Synthesis and Characterization:

Ru₄-5: To a 100 mL Schlenk flask fitted with a magnetic stir bar, thiophene-2,5-dicarboxylic acid (6.9 mg, 0.04 mmol, 1 equivalent), K_2CO_3 (6 mg, 0.04 mmol, one equivalent), and methanol (7 mL) were added. The mixture was stirred for 2 h. Subsequently, the methanolic solution of the dicarboxylate linker was added dropwise by cannula to the dichloroethane solution (7 mL) of the complex **Ru₂-3** (53 mg, 0.04 mmol, 1 equivalent). The reaction mixture was stirred at 45°C for 3 days. After cooling the reaction mixture to r. t., the solvents were evaporated to dryness. The crude mixture was dissolved in toluene and filtered. After evaporation of toluene, the residue was washed with methanol ($2 \times 5 \text{ mL}$). **Ru₄-5** was vacuum dried and finally obtained as a dark green solid.

Yield: 27.6 mg (0.0097 mmol, 49%).

^1H NMR (400 MHz, C_6D_6 ; for assignment of the resonance signals refer to Figure 10): δ in ppm = 10.11 (dd, $^3J_{\text{H,H}} = 7.0 \text{ Hz}$, $^4J_{\text{H,H}} = 1.9 \text{ Hz}$, 4H, H_4), 9.71 (d, $^3J_{\text{H,H}} = 15.2 \text{ Hz}$, 4H, H_1), 8.60 (d, $^3J_{\text{H,H}} = 15.2 \text{ Hz}$, 4H, H_2), 8.53 (4H, H_8), 7.95–7.85 (m, 8H, H_5 and H_6), 7.70 (s, 4H, H_3 or H_7), 7.54 (s, 4H, H_3 or H_7), 2.52–2.30 (m, 24H, H_9), and 1.51–1.15 (m, 144H, H_{10}).

$^{31}\text{P}\{^1\text{H}\}$ NMR (162 MHz, C_6D_6): δ in ppm = 38.62.

IR (CH_2Cl_2): 1906 cm^{-1} ($\nu_{\text{C}\equiv\text{O}}$).

ESI-MS (+ve ion mode), m/z : found at 1423.9248 (calcd for $[\text{M}]^{2+}$ for $\text{C}_{140}\text{H}_{200}\text{N}_4\text{O}_{12}\text{P}_8\text{Ru}_4\text{S}_2$ 1423.9371).

Ru₄-6: To a 100 mL Schlenk flask, fitted with a magnetic stir bar, isophthalic acid (2.3 mg, 0.0137 mmol, 1 equivalent), K_2CO_3 (3 mg, 0.02 mmol, 1.5 equivalents), and methanol (7 mL) were added. The mixture was stirred for 2 h. Subsequently, the methanolic solution of dicarboxylate linker was added dropwise into the dichloroethane solution (7 mL) of **Ru₂-3** (18.2 mg, 0.0137 mmol, 1 equivalent). The final reaction mixture was stirred at 45°C for

3 days. After cooling the reaction mixture to r. t., the solution was evaporated to dryness. The crude mixture was dissolved in dichloromethane and filtered. After evaporation of solvent, the residue was washed with methanol (1 × 5 mL) and hexane (1 × 5 mL). **Ru₄-6** was vacuum dried and, finally, obtained as a dark green solid.

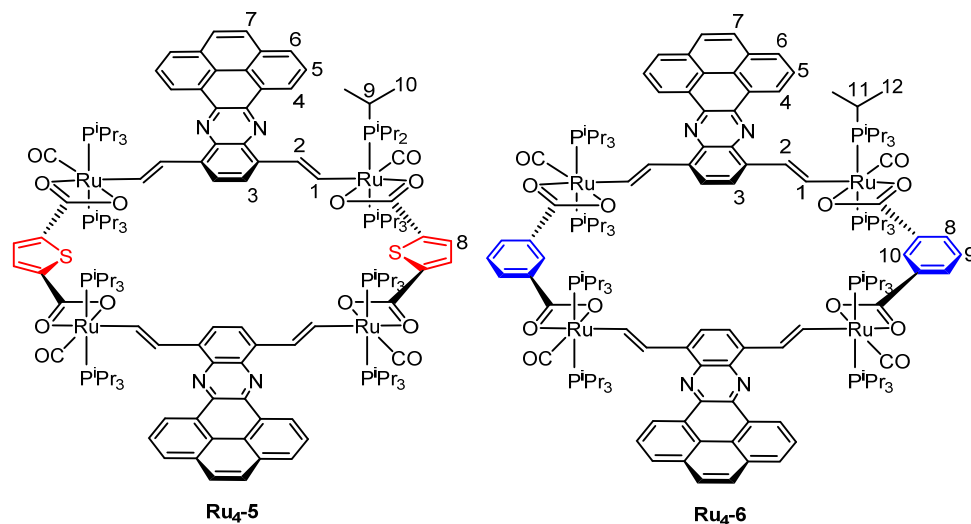


Figure 10. Atomic numbering for NMR characterization.

Yield: 10 mg (0.0035 mmol, 51%).

¹H NMR (400 MHz, C₆D₆; for assignment of the resonance signals refer to Figure 10): δ in ppm = 10.20 (dd, ³J_{H,H} = 7.7 Hz, ⁴J_{H,H} = 1.4 Hz, 4H, H₄), 9.74 (d, ³J_{H,H} = 15.5 Hz, 4H, H₁), 9.33 (s, 2H, H₁₀), 8.84 (d, ³J_{H,H} = 15.5 Hz, 4H, H₂), 8.47 (s, 4H, H₃ or H₇), 8.33 (dd, ³J_{H,H} = 7.7 Hz, ⁴J_{H,H} = 1.4 Hz, 2H, H₆), 8.02–7.86 (m, 10H, H_{5/8/9}), 7.73 (s, 4H, H₃ or H₇), 2.51–2.35 (m, 24H, H₁₁), 1.50–1.24 (m, 144H, H₁₂).

³¹P{¹H} NMR (162 MHz, C₆D₆): δ in ppm = 38.65.

IR (CH₂Cl₂): 1905 cm⁻¹ ($\nu_{C\equiv O}$).

ESI-MS (+ve ion mode), *m/z*: found at 1417.9691 (calcd. for the [M]²⁺ ion of **Ru₄-6**, 1417.9809).

Synthesis of CT-1: To a 50 mL Schlenk flask fitted with a magnetic bar, complex **Ru₄-5** (2.84 mg, 0.001 mmol, 1 equivalent) was dissolved in dichloromethane (2 mL). To this solution, a dichloromethane solution of F₄TCNQ (0.54 mg, 0.002 mmol, 2 equivalents) was added. An immediate colour change, from leafy-green to pale yellow-green, was observed. The solution was stirred for 5 min and evaporated to dryness to give **CT-1** ([**Ru₄-5**]²⁺ [F₄TCNQ]⁻)₂ in quantitate yield.

The salt was characterized by EPR, IR, and UV–vis–NIR spectroscopy (see Supplementary Materials).

Synthesis of CT-2: To a 50 mL Schlenk flask fitted with a magnetic bar, complex **Ru₄-6** (1.41 mg, 0.0005 mmol, 1 equivalent) was dissolved in dichloromethane (2 mL). To this solution, a dichloromethane solution of F₄TCNQ (0.27 mg, 0.001 mmol, 2 equivalents) was added. Immediate change of colour from dark green to dark yellow-green was observed. The solution was stirred for 5 min and evaporated to dryness to give **CT-2** ([**Ru₄-6**]²⁺ [F₄TCNQ]⁻)₂ in quantitate yield.

The salt was characterized by EPR, IR, and UV–vis–NIR spectroscopy (see Supplementary Materials).

5. Conclusions

We report on the tetraruthenium macrocycles **Ru₄-5** and **Ru₄-6**, which feature a 5,8-divinylquinoxaline linker with a laterally appended, annulated pyrene constituent. Both complexes and their various oxidized and reduced forms were characterized by NMR, MS, IR, UV–vis–NIR, and EPR spectroscopy. X-ray diffraction on a single crystal of the methanol

tetrasolvate of **Ru₄-5** shows that the macrocycle adopts a C_i symmetry and a somewhat wavy structure, due to an alternant tilting of the dicarboxylate and divinylphenylene linkers to above or below the planar Ru_4 rhomboid. An unusual feature is that hydrogen bonding of a methanol solvate molecule to the carbonyl oxygen donor of one carboxylate functionality of each linker weakens the corresponding Ru–O bond to almost unidentate carboxylate binding. The present structure thus provides a snapshot of solvent-assisted ligand substitution, as it is instrumental for the formation of such complex molecular architectures. The molecular packing in the crystal showed that the pyrene pendants, despite being sterically rather unencumbered, do not engage in intermolecular π -stacking interactions. Rather, several $CH \cdots \pi$ contacts to P^iPr_3 methyl groups of neighbouring molecules were formed.

Cyclic and square-wave voltammetric studies revealed that the complexes can be oxidized twice by the release of two electrons in each step, one from each divinylarylene linker. Both complexes can also be reduced by two electrons, due to the presence of two electron-accepting azaacene units. IR studies showed that the electron hole at each divinylphenylene linker of the dicationic complexes **[Ru₄-5]²⁺** and **[Ru₄-6]²⁺** is symmetrically distributed. However, in this particular case, the prominent low-energy NIR and vis bands of these mixed-valent species with two interlinked, open-shell **[Ru-CH=CH-quinoxaline-CH=CH-Ru]^{•+}** entities are better described as intraligand charge-transfer (ILCT) bands with an ensuing shift of electron density from the laterally appended pyrene constituent to the oxidized divinylphenylene diruthenium entity, rather than as conventional intervalence charge-transfer (IVCT) bands.

The low oxidation potentials of the tetraruthenium macrocycles also allows for the formation of radical charge-transfer (CT) salts with the strong organic electron acceptor F_4TCNQ . Their 1:2 CT salts are composed out of the dications of the macrocycles and two $F_4TCNQ^{\bullet-}$ anions, as was confirmed by IR, UV–vis–NIR, and EPR spectroscopy.

Supplementary Materials: The following supporting information can be downloaded at: <https://www.mdpi.com/article/10.3390/inorganics10060082/s1>, Figure S1: ¹H NMR spectrum of **Ru₄-5** in C_6D_6 ; Figure S2: ³¹P{¹H} NMR spectrum of **Ru₄-5** in C_6D_6 ; Figure S3: ¹H NMR spectrum of **Ru₄-6** in C_6D_6 (298 K); Figure S4: ³¹P{¹H} NMR spectrum of **Ru₄-6** in C_6D_6 ; Figure S5: High-resolution electrospray ionisation mass spectrum (HR ESI-MS) of **Ru₄-5** (+ve ion mode); Figure S6: Isotopic pattern of the molecular ion **[M]²⁺** peak of **Ru₄-5**; Figure S7: High-resolution electrospray ionisation mass spectrum (HR ESI-MS) of **Ru₄-6** (+ve ion mode); Figure S8: Isotopic pattern of the molecular ion **[M]²⁺** peak of **Ru₄-6**; Figure S9: The intermolecular hydrogen bonding interactions with the co-crystallized solvent methanol molecules to one of the carboxylate functional groups of **Ru₄-5**; Figure S10: Cyclic voltammogram of **Ru₄-3** at $v = 100$ mV/s in CH_2Cl_2 ; Figure S11: Cyclic (left) ($v = 100$ mV/s) and square-wave voltammograms (right) of **Ru₄-5**; Figure S12: Cyclic (left) ($v = 100$ mV/s) and square-wave voltammograms (right) of **Ru₄-5** in CH_2Cl_2 ; Figure S13: Simulated cyclic voltammogram ($v = 400$ mV/s) of the two oxidation waves of **Ru₄-5**; Figure S14: Cyclic (left) ($v = 100$ mV/s) and square-wave voltammograms (right) of **Ru₄-6** in THF; Figure S15: Cyclic (left) ($v = 100$ mV/s) and square-wave voltammograms (right) of **Ru₄-6** in CH_2Cl_2 ; Figure S16: Simulated cyclic voltammogram ($v = 100$ mV/s) of the two oxidation waves of **Ru₄-6**; Figure S17: Changes in the mid-IR [Ru(CO)] spectra of **Ru₄-5** upon oxidation from **Ru₄-5** to **[Ru₄-5]²⁺** and second oxidation from **[Ru₄-5]²⁺** to **[Ru₄-5]⁴⁺** in CH_2Cl_2 ; Figure S18: Deconvoluted IR spectrum ([Ru(CO)]) of **[Ru₄-5]²⁺**; Figure S19: Spectroscopic changes in the NIR region upon oxidation of **Ru₄-5** to **[Ru₄-5]²⁺** and **[Ru₄-5]⁴⁺** in CH_2Cl_2 ; Figure S20: Spectroscopic changes in the UV–vis–NIR region upon oxidation of **Ru₄-5** to **[Ru₄-5]²⁺** and **[Ru₄-5]⁴⁺** in CH_2Cl_2 ; Figure S21: Spectroscopic changes in the UV–vis–NIR region upon oxidation of **Ru₄-5** to **[Ru₄-5]²⁺** in CH_2Cl_2 ; Figure S22: Changes in the mid-IR [Ru(CO)] spectra of **Ru₄-6** upon oxidation from **Ru₄-6** to **[Ru₄-6]²⁺** and **[Ru₄-6]⁴⁺** in CH_2Cl_2 ; Figure S23: Deconvoluted [Ru(CO)] spectrum of **[Ru₄-6]²⁺**; Figure S24: Spectroscopic changes in the NIR region upon oxidation of **Ru₄-6** to **[Ru₄-6]²⁺** and **[Ru₄-6]⁴⁺** in CH_2Cl_2 ; Figure S25: Spectroscopic changes in the UV–vis–NIR region upon oxidation of **Ru₄-6** to **[Ru₄-6]²⁺** and **[Ru₄-6]⁴⁺** in CH_2Cl_2 ; Figure S26: Contour plots of the calculated HOMO, HOMO-1, LUMO, and LUMO+1 of model complex **MeRu₂-3**; Figure S27: Calculated UV–vis–NIR spectrum of **[MeRu₂-3]²⁺** in its electronic singlet state; Figure S28: EPR Spectra of **[Ru₄-5]²⁺** and **[Ru₄-5]⁴⁺**; Figure S29: EPR Spectra of **[Ru₄-6]²⁺**

and $[\text{Ru}_4\text{-6}]^{4+}$; Figure S30: EPR Spectra of $[\text{Ru}_4\text{-5}]^{2+}$ and $[\text{Ru}_4\text{-6}]^{2+}$ measured at 298K; Figure S31: Computed spin densities for the radical anion (left), cation (middle), and dication (right, triplet state) of the model for complex **Ru₂-3**; Figure S32: Charge-transfer salts **CT-1 (A)** and **CT-2 (B)**; Figure S33: Monitoring the formation of salt **CT-1 (1:2 mixture of Ru₄-5 and F₄TCNQ)** through IR spectroscopy; Figure S34: Monitoring the formation of salt **CT-2 (1:2 mixture of Ru₄-6 and F₄TCNQ)** through IR spectroscopy; Figure S35: The UV-vis-NIR spectrum of **CT-2 salt (1:2 mixture of Ru₄-6 and F₄TCNQ)**, together with those of the neutral complex, neutral F₄TCNQ, oxidized complex $[\text{Ru}_4\text{-6}]^{2+}$, and mono-reduced F₄TCNQ; Figure S36: EPR spectrum of salt **CT-2**; Figure S37. Powder X-ray diffraction (PXRD) pattern of the charge-transfer salt **CT-1** ($[\text{Ru}_4\text{-5}]^{2+} [\text{F}_4\text{TCNQ}]_2^-$); Figure S38. Powder X-ray diffraction (PXRD) pattern of the charge-transfer salt **CT-2** ($[\text{Ru}_4\text{-6}]^{2+} [\text{F}_4\text{TCNQ}]_2^-$). Table S1: Crystal data and structure refinement for **Ru₄-5**; Table S2: Data of cyclic voltammetric measurements of tetraruthenium macrocycle **Ru₄-5** at different scan rates in THF/ⁿBu₄NPF₆; Table S3: Data of cyclic voltammetric measurements of tetraruthenium macrocycle **Ru₄-6** at different scan rates in THF/ⁿBu₄NPF₆.

Author Contributions: Conceptualization, R.D. and R.F.W.; preparative electrochemical and spectroelectrochemical studies R.D.; X-ray and computational studies M.L.; mass spectrometry: L.S.; resources: I.I.-B. and R.F.W.; writing—original draft preparation, R.D. and R.F.W.; writing—review and editing, R.D., M.L. and R.F.W. All authors have read and agreed to the published version of the manuscript.

Funding: We gratefully acknowledge the financial support of this work by the Deutsche Forschungsgemeinschaft (DFG), through grant number Wi1232/17-1. The authors also acknowledge the support by the state of Baden-Wuerttemberg, through bwHPC, and Deutsche Forschungsgemeinschaft (DFG), through grant number INST 40/575-1 FUGG (JUSTUS 2 cluster).

Institutional Review Board Statement: Not applicable.

Informed Consent Statement: Not applicable.

Data Availability Statement: All the data used in this paper, were either available in the main paper or Supplementary Material section.

Acknowledgments: We wish to thank our colleague Miriam M. Unterlass and Hipassia Moura for conducting the powder X-ray diffraction measurements on salts **CT-1** and **-2**.

Conflicts of Interest: The authors declare no conflict of interest.

Sample Availability: Samples are available from the authors.

References

1. Cook, T.R.; Stang, P.J. Recent Developments in the Preparation and Chemistry of Metallacycles and Metallacages via Coordination. *Chem. Rev.* **2015**, *115*, 7001–7045. [[CrossRef](#)] [[PubMed](#)]
2. Chakrabarty, R.; Mukherjee, P.S.; Stang, P.J. Supramolecular coordination: Self-assembly of finite two- and three-dimensional ensembles. *Chem. Rev.* **2011**, *111*, 6810–6918. [[CrossRef](#)] [[PubMed](#)]
3. Fujita, M.; Tominaga, M.; Hori, A.; Therrien, B. Coordination Assemblies from a Pd(II)-Cornered Square Complex. *Acc. Chem. Res.* **2005**, *38*, 369–378. [[CrossRef](#)] [[PubMed](#)]
4. Szalóki, G.; Croué, V.; Carré, V.; Aubriet, F.; Alévêque, O.; Levillain, E.; Allain, M.; Aragón, J.; Ortí, E.; Goeb, S.; et al. Controlling the Host–Guest Interaction Mode through a Redox Stimulus. *Angew. Chem. Int. Ed.* **2017**, *56*, 16272–16276. [[CrossRef](#)] [[PubMed](#)]
5. Szaloki, G.; Croué, V.; Allain, M.; Goeb, S.; Salle, M. Neutral versus polycationic coordination cages: A comparison regarding neutral guest inclusion. *Chem. Commun.* **2016**, *52*, 10012–10015. [[CrossRef](#)]
6. Freudenreich, J.; Dalvit, C.; Süß-Fink, G.; Therrien, B. Encapsulation of Photosensitizers in Hexa- and Octanuclear Organometallic Cages: Synthesis and Characterization of Carceplex and Host–Guest Systems in Solution. *Organometallics* **2013**, *32*, 3018–3033. [[CrossRef](#)]
7. Barry, N.P.E.; Zava, O.; Dyson, P.J.; Therrien, B. Encapsulation of inorganic and organic guest molecules into an organometallic hexacationic arene osmium metalla-prism: Synthesis, characterisation and anticancer activity. *J. Organomet. Chem.* **2012**, *705*, 1–6. [[CrossRef](#)]
8. Ward, M.D.; Hunter, C.A.; Williams, N.H. Coordination Cages Based on Bis(pyrazolylpyridine) Ligands: Structures, Dynamic Behavior, Guest Binding, and Catalysis. *Acc. Chem. Res.* **2018**, *51*, 2073–2082. [[CrossRef](#)]
9. Pluth, M.D.; Raymond, K.N. Reversible guest exchange mechanisms in supramolecular host-guest assemblies. *Chem. Soc. Rev.* **2007**, *36*, 161–171. [[CrossRef](#)]

10. Fujii, S.; Tada, T.; Komoto, Y.; Osuga, T.; Murase, T.; Fujita, M.; Kiguchi, M. Rectifying Electron-Transport Properties through Stacks of Aromatic Molecules Inserted into a Self-Assembled Cage. *J. Am. Chem. Soc.* **2015**, *137*, 5939–5947. [[CrossRef](#)]
11. Kiguchi, M.; Ohto, T.; Fujii, S.; Sugiyasu, K.; Nakajima, S.; Takeuchi, M.; Nakamura, H. Single Molecular Resistive Switch Obtained via Sliding Multiple Anchoring Points and Varying Effective Wire Length. *J. Am. Chem. Soc.* **2014**, *136*, 7327–7332. [[CrossRef](#)] [[PubMed](#)]
12. Kiguchi, M.; Takahashi, T.; Takahashi, Y.; Yamauchi, Y.; Murase, T.; Fujita, M.; Tada, T.; Watanabe, S. Electron Transport through Single Molecules Comprising Aromatic Stacks Enclosed in Self-Assembled Cages. *Angew. Chem. Int. Ed.* **2011**, *50*, 5708–5711. [[CrossRef](#)] [[PubMed](#)]
13. Chen, H.; Fraser Stoddart, J. From molecular to supramolecular electronics. *Nat. Rev. Mater.* **2021**, *6*, 804–828. [[CrossRef](#)]
14. Das, R.; Linseis, M.; Schupp, S.M.; Schmidt-Mende, L.; Winter, R.F. Electron-Rich Diruthenium Complexes with π -Extended Alkenyl Ligands and Their F₄TCNQ Charge-Transfer Salts. *Chem. Eur. J.* **2022**, *28*, e202104403. [[CrossRef](#)] [[PubMed](#)]
15. Fink, D.; Weibert, B.; Winter, R.F. Redox-active tetraruthenium metallocycles: Reversible release of up to eight electrons resulting in strong electrochromism. *Chem. Commun.* **2016**, *52*, 6103–6106. [[CrossRef](#)]
16. Fink, D.; Bodensteiner, M.; Linseis, M.; Winter, R.F. Macrocyclic Triruthenium Complexes Having Electronically Coupled Mixed-Valent States. *Chem. Eur. J.* **2018**, *24*, 992–996. [[CrossRef](#)]
17. Scheerer, S.; Linseis, M.; Wuttke, E.; Weickert, S.; Drescher, M.; Troppner, O.; Ivanovic-Burmazovic, I.; Irmeler, A.; Pauly, F.; Winter, R.F. Redox-Active Tetraruthenium Macrocycles Built from 1,4-Divinylphenylene-Bridged Diruthenium Complexes. *Chem. Eur. J.* **2016**, *22*, 9574–9590. [[CrossRef](#)]
18. Fink, D.; Orth, N.; Linseis, M.; Ivanovic-Burmazovic, I.; Winter, R.F. Ring size matters: Supramolecular isomerism in self-assembled redox-active tetra- and hexaruthenium macrocycles. *Chem. Commun.* **2020**, *56*, 1062–1065. [[CrossRef](#)]
19. Fink, D.; Orth, N.; Linseis, M.; Ivanović-Burmazović, I.; Winter, R.F. Structural Versatility and Supramolecular Isomerism in Redox-Active Tetra- and Hexaruthenium Macrocycles. *Eur. J. Inorg. Chem.* **2020**, *2020*, 2816–2829. [[CrossRef](#)]
20. Rotthowe, N.; Linseis, M.; Vogelsang, L.; Orth, N.; Ivanović-Burmazović, I.; Winter, R.F. A “Pretender” Croconate-Bridged Macrocyclic Tetraruthenium Complex: Sizable Redox Potential Splittings despite Electronically Insulated Divinylphenylene Diruthenium Entities. *Molecules* **2021**, *26*, 5232. [[CrossRef](#)]
21. Fujita, M.; Sasaki, O.; Mitsunashi, T.; Fujita, T.; Yazaki, J.; Yamaguchi, K.; Ogura, K. On the structure of transition-metal-linked molecular squares. *Chem. Commun.* **1996**, *13*, 1535–1536. [[CrossRef](#)]
22. Suzuki, K.; Kawano, M.; Fujita, M. Solvato-Controlled Assembly of Pd₃L₆ and Pd₄L₈ Coordination “Boxes”. *Angew. Chem. Int. Ed.* **2007**, *46*, 2819–2822. [[CrossRef](#)] [[PubMed](#)]
23. Frisch, M.J.; Trucks, G.W.; Schlegel, H.B.; Scuseria, G.E.; Robb, M.A.; Cheeseman, J.R.; Scalmani, G.; Barone, V.; Petersson, G.A.; Nakatsuji, H.; et al. *Gaussian 09*; Revision D.01; Gaussian, Inc.: Wallingford, CT, USA, 2009.
24. Beves, J.E.; Blight, B.A.; Campbell, C.J.; Leigh, D.A.; McBurney, R.T. Strategies and tactics for the metal-directed synthesis of rotaxanes, knots, catenanes, and higher order links. *Angew. Chem. Int. Ed.* **2011**, *50*, 9260–9327. [[CrossRef](#)] [[PubMed](#)]
25. Neogi, S.; Lorenz, Y.; Engeser, M.; Samanta, D.; Schmittel, M. Heteroleptic Metallosupramolecular Racks, Rectangles, and Trigonal Prisms: Stoichiometry-Controlled Reversible Interconversion. *Inorg. Chem.* **2013**, *52*, 6975–6984. [[CrossRef](#)] [[PubMed](#)]
26. Rancan, M.; Dolmella, A.; Seraglia, R.; Orlandi, S.; Quici, S.; Armelao, L. A templating guest sorts out a molecular triangle from a dimer–trimer constitutional dynamic library. *Chem. Commun.* **2012**, *48*, 3115–3117. [[CrossRef](#)]
27. Wang, W.; Wang, Y.-X.; Yang, H.-B. Supramolecular transformations within discrete coordination-driven supramolecular architectures. *Chem. Soc. Rev.* **2016**, *45*, 2656–2693. [[CrossRef](#)]
28. Garci, A.; Marti, S.; Schurch, S.; Therrien, B. Insight into the dynamic ligand exchange process involved in bipyridyl linked arene ruthenium metalla-rectangles. *RSC Adv.* **2014**, *4*, 8597–8604. [[CrossRef](#)]
29. Goswami, A.; Saha, S.; Biswas, P.K.; Schmittel, M. (Nano)mechanical Motion Triggered by Metal Coordination: From Functional Devices to Networked Multicomponent Catalytic Machinery. *Chem. Rev.* **2020**, *120*, 125–199. [[CrossRef](#)]
30. Anyfanti, G.; Bauza, A.; Gentiluomo, L.; Rodrigues, J.; Portalone, G.; Frontera, A.; Rissanen, K.; Puttreddy, R. Short X... N Halogen Bonds With Hexamethylenetetraamine as the Acceptor. *Front. Chem.* **2021**, *9*, 623595. [[CrossRef](#)]
31. Dang, L.-L.; Feng, H.-J.; Lin, Y.-J.; Jin, G.-X. Self-Assembly of Molecular Figure-Eight Knots Induced by Quadruple Stacking Interactions. *J. Am. Chem. Soc.* **2020**, *142*, 18946–18954. [[CrossRef](#)]
32. Gao, X.; Cui, Z.; Shen, Y.-R.; Liu, D.; Lin, Y.-J.; Jin, G.-X. Synthesis and Near-Infrared Photothermal Conversion of Discrete Supramolecular Topologies Featuring Half-Sandwich [Cp*Rh] Units. *J. Am. Chem. Soc.* **2021**, *143*, 17833–17842. [[CrossRef](#)] [[PubMed](#)]
33. Zhang, J.; Xu, W.; Sheng, P.; Zhao, G.; Zhu, D. Organic Donor-Acceptor Complexes as Novel Organic Semiconductors. *Acc. Chem. Res.* **2017**, *50*, 1654–1662. [[CrossRef](#)] [[PubMed](#)]
34. Wang, W.; Luo, L.; Sheng, P.; Zhang, J.; Zhang, Q. Multifunctional Features of Organic Charge-Transfer Complexes: Advances and Perspectives. *Chem. Eur. J.* **2021**, *27*, 464–490. [[CrossRef](#)] [[PubMed](#)]
35. Goetz, K.P.; Vermeulen, D.; Payne, M.E.; Kloc, C.; McNeil, L.E.; Jurchescu, O.D. Charge-transfer complexes: New perspectives on an old class of compounds. *J. Mater. Chem. C* **2014**, *2*, 3065–3076. [[CrossRef](#)]
36. Bassler, H.; Kohler, A. Charge transport in organic semiconductors. *Top. Curr. Chem.* **2012**, *312*, 1–65. [[CrossRef](#)]
37. Wosnitza, J. Superconductivity in Layered Organic Metals. *Crystals* **2012**, *2*, 248–265. [[CrossRef](#)]

38. Fink, D.; Orth, N.; Ebel, V.; Gogesch, F.S.; Staiger, A.; Linseis, M.; Ivanović-Burmazović, I.; Winter, R.F. Self-Assembled Redox-Active Tetraruthenium Macrocycles with Large Intracyclic Cavities. *Organometallics* **2020**, *39*, 1861–1880. [[CrossRef](#)]
39. Rudolph, M.; Feldberg, S. *DigiSim3*; Version 3.03; Bioanalytical Systems, Inc.: West Lafayette, IN, USA, 1994.
40. Fink, D.; Linseis, M.; Winter, R.F. Constitutional Isomers of Macrocyclic Tetraruthenium Complexes with Vastly Different Spectroscopic and Electrochemical Properties. *Organometallics* **2018**, *37*, 1817–1820. [[CrossRef](#)]
41. Fink, D.; Staiger, A.; Orth, N.; Linseis, M.; Ivanovic-Burmazovic, I.; Winter, R.F. Redox-Induced Hydrogen Bond Reorientation Mimicking Electronic Coupling in Mixed-Valent Diruthenium and Macrocyclic Tetraruthenium Complexes. *Inorg. Chem.* **2020**, *59*, 16703–16715. [[CrossRef](#)]
42. Sherlock, S.J.; Boyd, D.C.; Moasser, B.; Gladfelter, W.L. Homogeneous catalytic carbonylation of nitroaromatics. 4. Preparation and characterization of ruthenium radical cations. *Inorg. Chem.* **1991**, *30*, 3626–3632. [[CrossRef](#)]
43. Maurer, J.; Winter, R.F.; Sarkar, B.; Fiedler, J.; Zališ, S. Bridge dominated oxidation of a diruthenium 1,3-divinylphenylene complex. *Chem. Commun.* **2004**, *17*, 1900–1901. [[CrossRef](#)] [[PubMed](#)]
44. Maurer, J.; Sarkar, B.; Schwederski, B.; Kaim, W.; Winter, R.F.; Zališ, S. Divinylphenylene-Bridged Diruthenium Complexes Bearing Ru(CO)Cl(PⁱPr₃)₂ Entities. *Organometallics* **2006**, *25*, 3701–3712. [[CrossRef](#)]
45. Mücke, P.; Linseis, M.; Zališ, S.; Winter, R.F. Vinyl-ruthenium entities as markers for intramolecular electron transfer processes. *Inorg. Chim. Acta* **2011**, *374*, 36–50. [[CrossRef](#)]
46. Scheerer, S.; Rotthowe, N.; Abdel-Rahman, O.S.; He, X.; Rigaut, S.; Kvapilova, H.; Zalis, S.; Winter, R.F. Vinyl ruthenium-modified biphenyl and 2,2'-bipyridines. *Inorg. Chem.* **2015**, *54*, 3387–3402. [[CrossRef](#)] [[PubMed](#)]
47. Linseis, M.; Zalis, S.; Zabel, M.; Winter, R.F. Ruthenium stilbenyl and diruthenium distyrylethene complexes: Aspects of electron delocalization and electrocatalyzed isomerization of the Z-isomer. *J. Am. Chem. Soc.* **2012**, *134*, 16671–16692. [[CrossRef](#)]
48. Rotthowe, N.; Zwicker, J.; Winter, R.F. Influence of Quinoidal Distortion on the Electronic Properties of Oxidized Divinylarylene-Bridged Diruthenium Complexes. *Organometallics* **2019**, *38*, 2782–2799. [[CrossRef](#)]
49. Krejčík, M.; Daněk, M.; Hartl, F. Simple construction of an infrared optically transparent thin-layer cell: Applications to the redox reactions of ferrocene, Mn₂(CO)₁₀ and Mn(CO)₃(3,5-di-t-butyl-catecholate). *J. Electroanal. Chem. Interfac. Electrochem.* **1991**, *317*, 179–187. [[CrossRef](#)]
50. Connelly, N.G.; Geiger, W.E. Chemical Redox Agents for Organometallic Chemistry. *Chem. Rev.* **1996**, *96*, 877–910. [[CrossRef](#)]
51. Zhang, J.; Liu, G.; Zhou, Y.; Long, G.; Gu, P.; Zhang, Q. Solvent Accommodation: Functionalities Can Be Tailored through Co-Crystallization Based on 1:1 Coronene-F₄TCNQ Charge-Transfer Complex. *ACS Appl. Mater. Interfaces* **2017**, *9*, 1183–1188. [[CrossRef](#)]
52. Hu, P.; Li, H.; Li, Y.; Jiang, H.; Kloc, C. Single-crystal growth, structures, charge transfer and transport properties of anthracene-F₄TCNQ and tetracene-F₄TCNQ charge-transfer compounds. *CrystEngComm* **2017**, *19*, 618–624. [[CrossRef](#)]
53. Cochran, J.E.; Junk, M.J.N.; Glauddell, A.M.; Miller, P.L.; Cowart, J.S.; Toney, M.F.; Hawker, C.J.; Chmelka, B.F.; Chabynyc, M.L. Molecular Interactions and Ordering in Electrically Doped Polymers: Blends of PBTTT and F₄TCNQ. *Macromolecules* **2014**, *47*, 6836–6846. [[CrossRef](#)]
54. Le, T.H.; Nafady, A.; Vo, N.T.; Elliott, R.W.; Hudson, T.A.; Robson, R.; Abrahams, B.F.; Martin, L.L.; Bond, A.M. Electrochemically directed synthesis of Cu₂(I)(TCNQF₄(II⁻))(MeCN)₂ (TCNQF₄ = 2,3,5,6-tetrafluoro-7,7,8,8-tetracyanoquinodimethane): Voltammetry, simulations, bulk electrolysis, spectroscopy, photoactivity, and X-ray crystal structure of the Cu₂(I)(TCNQF₄(II))(EtCN)₂ analogue. *Inorg. Chem.* **2014**, *53*, 3230–3242. [[CrossRef](#)] [[PubMed](#)]
55. Pingel, P.; Neher, D. Comprehensive picture of p-type doping of P3HT with the molecular acceptor F₄TCNQ. *Phys. Rev. B* **2013**, *87*, 115209. [[CrossRef](#)]
56. O’Kane, S.A.; Clérac, R.; Zhao, H.; Ouyang, X.; Galán-Mascarós, J.R.; Heintz, R.; Dunbar, K.R. New Crystalline Polymers of Ag(TCNQ) and Ag(TCNQF₄): Structures and Magnetic Properties. *J. Solid State Chem.* **2000**, *152*, 159–173. [[CrossRef](#)]
57. Le, T.H.; Nafady, A.; Lu, J.; Peleckis, G.; Bond, A.M.; Martin, L.L. Electrochemical Synthesis and Characterization of Semiconducting Ni(TCNQF₄)₂(H₂O)₂ (TCNQF₄ = 2,3,5,6-tetrafluoro-7,7,8,8-tetracyanoquinodimethane). *Eur. J. Inorg. Chem.* **2012**, *2012*, 2889–2897. [[CrossRef](#)]
58. Murata, T.; Saito, G.; Nakamura, K.; Maesato, M.; Hiramatsu, T.; Yoshida, Y. Exploration of Charge-Transfer Solids Utilizing Nucleobases: Nanoarchitectures by Hydrogen-Bonds in the Ionic Assemblies of Guanine and TCNQ Derivatives. *Cryst. Growth Des.* **2013**, *13*, 2778–2792. [[CrossRef](#)]
59. Gerson, F.; Heckendorn, R.; Cowan, D.O.; Kini, A.M.; Maxfield, M. Radical anions and radical trianions of tetracyanoarenoquinodimethanes. An ESR and ENDOR study. *J. Am. Chem. Soc.* **1983**, *105*, 7017–7023. [[CrossRef](#)]
60. Jones, M.T.; Maruo, T.; Jansen, S.; Roble, J.; Rataiczak, R.D. Comparative ESR Studies of Solid Polycrystalline Alkali Metal Salts of TCNQ and TCNQF₄. *Mol. Cryst. Liq. Cryst.* **1986**, *134*, 21–30. [[CrossRef](#)]
61. Stoll, S.; Schweiger, A. EasySpin, a comprehensive software package for spectral simulation and analysis in EPR. *J. Magn. Reson.* **2006**, *178*, 42–55. [[CrossRef](#)]
62. Dolomanov, O.V.; Bourhis, L.J.; Gildea, R.J.; Howard, J.A.K.; Puschmann, H. OLEX2: A complete structure solution, refinement and analysis program. *J. Appl. Cryst.* **2009**, *42*, 339–341. [[CrossRef](#)]
63. Sheldrick, G.M. Crystal structure refinement with SHELXL. *Acta Cryst. C* **2015**, *7*, 3–8. [[CrossRef](#)] [[PubMed](#)]
64. Farrugia, L.J. WinGXandORTEP for Windows: An update. *J. Appl. Cryst.* **2012**, *45*, 849–854. [[CrossRef](#)]

65. Mennucci, B.; Tomasi, J. A consistent and accurate ab initio parametrization of density functional dispersion correction (DFT-D) for the 94 elements H-Pu. *J. Chem. Phys.* **2010**, *132*, 154104. [[CrossRef](#)]
66. Cossi, M.; Rega, N.; Scalmani, G.; Barone, V. Energies, structures, and electronic properties of molecules in solution with the C-PCM solvation model. *J. Comput. Chem.* **2003**, *24*, 669–681. [[CrossRef](#)] [[PubMed](#)]
67. Dolg, M.; Stoll, H.; Preuss, H. Energy-adjusted ab initio pseudopotentials for the rare earth elements. *J. Chem. Phys.* **1989**, *90*, 1730–1734. [[CrossRef](#)]
68. Küchle, W.; Dolg, M.; Stoll, H.; Preuss, H. Energy-adjusted pseudopotentials for the actinides. Parameter sets and test calculations for thorium and thorium monoxide. *J. Chem. Phys.* **1994**, *100*, 7535–7542. [[CrossRef](#)]
69. Andrae, D.; Haeussermann, U.; Dolg, M.; Stoll, H.; Preuss, H. Energy-adjusted ab initio pseudopotentials for the second and third row transition elements. *Theor. Chim. Acta* **1990**, *77*, 123–141. [[CrossRef](#)]
70. Hariharan, P.H.; Pople, J.A. The Influence of Polarization Functions on Molecular Orbital Hydrogenation Energies. *Theor. Chim. Acta* **1973**, *28*, 213–222. [[CrossRef](#)]
71. Perdew, J.P.; Burke, K.; Ernzerhof, M. Generalized Gradient Approximation Made Simple. *Phys. Rev. Lett.* **1996**, *77*, 3865–3868. [[CrossRef](#)]
72. Adamo, C.; Barone, V. Semiempirical hybrid density functional with perturbative second-order correlation. *J. Chem. Phys.* **2006**, *124*, 6158–6170. [[CrossRef](#)]
73. O’Boyle, N.M.; Tenderholt, A.L.; Langner, K.M. cclib: A library for package-independent computational chemistry algorithms. *J. Comput. Chem.* **2008**, *29*, 839–845. [[CrossRef](#)] [[PubMed](#)]
74. Hanwell, M.D.; Curtis, D.E.; Lonie, D.C.; Vandermeersch, T.; Zurek, E.; Hutchison, G.R. Avogadro: An advanced semantic chemical editor, visualization, and analysis platform. *J. Cheminf.* **2012**, *4*, 17. [[CrossRef](#)] [[PubMed](#)]
75. Tange, O. GNU Parallel—The Command-Line Power Tool. *USENIX Mag.* **2011**, *36*, 42–47.
76. Humphrey, W.; Dalke, A.; Schulten, K. VMD: Visual molecular dynamics. *J. Mol. Graph.* **1996**, *14*, 33–38. [[CrossRef](#)]
77. *Persistence of Vision Raytracer*; Version 3.7; Persistence of Vision Raytracer Pty. Ltd.: Williamstown, Australia, 2004.